PIPERIDINIUM BASED IONIC LIQUID – SILICA NANOPARTICLE HYBRID ELECTROLYTE FOR LITHIUM METAL BATTERIES

A Thesis

Presented to the Faculty of the Graduate School

of Cornell University

In Partial Fulfillment of the Requirements for the Degree of

Master of Science

by

Kevin Stephen Korf

January 2014

ABSTRACT

Herein is reported a novel piperidinium tethered silica nanoparticle hybrid electrolyte with 1M LiTFSI and PC for use in lithium metal batteries. This unique NOHMs electrolyte provides a solid-like physical barrier to dendritic growth due to the jamming phase transition while maintaining use of the piperidinium chemistry to achieve the same effect. Through a battery of characterizations, it was found that the tethered electrolyte displayed thermal stability up to 380 °C, high conductivities that were weakly affected by increases in viscosity and followed a VFT fit, low interfacial resistances, could be tuned to exhibit MPa scale moduli, and had an SEI layer that was able to efficiently stem dendritic growth. Polarization experiments of lithium symmetric cells showed long short circuit times whereas cycling experiments of symmetric cells showed no sign of short circuit, even after 1000 hours. Using a carbon modified lithium titanate counterelectrode, the cell exhibited stable voltage plateaus indicating electrolyte robustness during battery operation, capacity retentions of 87% over 1000 cycles, and no short circuit over 2000 cycles.

BIOGRAPHICAL SKETCH

Kevin Stephen Korf was born in Glendale, Arizona on December 9, 1988 and grew up in Scottsdale, Arizona. Kevin cherishes his family life; his mother is one of eight children and with his many cousins by his side, there was never a dull moment in his childhood life. He lived across the street from his aunt and just across town from his cousin and her family, facilitating a close knit family. There was never a family member to which he couldn't turn. In 2002 he was awarded the Mathematics Talent Search award by John Hopkins University for being among the highest scoring participants in the state of Arizona, kick starting his interest in mathematics and science. Originally planning to become a Doctor of Medicine, his undergraduate career soon showed him his true interest lie in engineering. In 2010, his internship as a Flammability Engineer at C&D Zodiac Aerospace and encouragement from a close friend inspired an interest in Materials Science, paving his path to study materials at Cornell University. Due in large part to his sunny life in Arizona, Kevin sought to study solar energy but soon found an equal interest in energy storage. When not working or performing research, he can be found watching or participating in sports, playing piano, video games, board games, reading, or simply relaxing with his family and two dogs.

ACKNOWLEDGMENTS

I would like to thank my advisor, Lynden Archer, for his patience, guidance, and support throughout my graduate career. I understand the frustration that must accompany the constant answering of the most basic and trifling questions. Thank you for always pointing me in the right direction when I wander astray.

I would also like to acknowledge my group members for their support and suggestions; particularly Yingying Lu and Jennifer Schaeffer, from whom I have learned so much and without whom completing this degree would have been impossible. I would further like to thank KAUST-CU for the wonderful facilities and equipment provided to enable me to effectively perform research.

Finally, I would like to thank all members of my caring family who have formed me into the person I am today, academically, emotionally, and personally. I would like to specifically thank my dad, Stephen Korf, for his ability to solve any of my problems at a moment's notice even over the phone, and my mom, Sharon Korf, for her frustratingly excessive support that was unknowingly a vital component of my academic life. In the end, it was very much appreciated. I love you all.

TABLE OF CONTENTS

LIST OF FIGURES

LIST OF TABLES

LIST OF ABBREVIATIONS

LiTFSI	Lithium bis(trifluoromethylsulfonyl)imide
PP13-TFSI	1-methyl-1-propyl piperidinium bis(trifluoromethylsulfonyl)imide
P13-TFSI	1-methyl-1-propyl pyrrolidinium bis(trifluoromethylsulfonyl)imide
SEI	Solid Electrolyte Interphase
NOHMs	Nanoscale Organic Hybrid Materials
OCP	Open Circuit Potential
DMF	Dimethylformamide
PC	Propylene Carbonate
TGA	Thermal Gravitational Analysis
NMR	Nuclear Magnetic Resonance
DMSO	Dimethyl sulfoxide
IL	Ionic Liquid
DI	Deionized
SEM	Scanning Electron Microscopy
EDX	Energy Dispersive X-ray Spectroscopy
VFT	Vogel-Fulcher-Tammann
DSC	Differential Scanning Calorimeter
LTO	Carbon Modified Lithium Titanate
SiO_2-PP-TFSI	Piperidinium tethered silica nanoparticle with TFSI as the paired anion

CHAPTER 1

INTRODUCTION

1.1 Background

Secondary lithium metal battery research has been a prime focus in recent years due to the energy and power needs of advancing technologies. A lithium metal battery is characterized by a variety of possibilities to be used as the cathode, such as elemental sulfur in lithium sulfur batteries[1] or open air in lithium-air batteries,[2] and an anode made of pure lithium metal separated by a liquid or solid-state electrolyte. Current lithium ion batteries are able to practically deliver a gravimetric energy density of 370 mA h g^{-1}, but the highest energy density possible for lithium ion batteries is still lacking for future long-range electric and hybrid vehicles.[3,5] It has long been known that disposing of the operation inactive, carbonaceous anode material that is present in lithium ion batteries would boost the overall energy density of the battery by over ten-fold, improving to around 3860 mA h g^{-1} theoretical.[3,4] Lithium-air batteries are even theoretically capable of delivering an energy density of 11,140 Wh kg^{-1}, comparable to that of gasoline, a goal that is ideal for future fully electric vehicles.[6]

Currently developing technologies such as hybrid and electric vehicles, cellular phones, laptops, and tablets all require batteries that are safe to use, stable, have high energy and power densities, and are inexpensive to manufacture. Lithium metal batteries have the highest gravimetric and volumetric energy densities of all preexisting battery technologies, are stable, and if paired with a proper cathode material, can exhibit high power densities.[3] Research on lithium metal batteries first started in the early 1970's, when Exxon began using TiS_2 as the

cathode and Li metal as the anode. However, it was then discovered that the system succumbed to the safety issue of all lithium metal batteries, dendritic lithium growth.[3,4]

Since then, lithium metal battery research has been focused on developing a system to prevent dendrite growth while still maintaining the necessary properties for proper battery function, such as conductivity, energy density, and power density. Dendritic growth occurs when operation active lithium ions deposit unevenly on the lithium metal anode, resulting in a deposit of inactive lithium metal. Over many charge cycles, this build up of lithium metal creates an arborescent structure which eventually spans the electrodes, resulting in short circuit.[1] The short circuit then leads to rapid overheating which in turn causes flame and with certain electrolytes, explosion hazards.[9] This dangerous occurrence has been the main cause of Li metal battery's absence from the market.

1.2 Choosing an Electrolyte

An electrolyte for a battery must meet certain requirements in order to perform properly in an electrolytic cell**.** First, it should promote ion pair dissociation and facilitate transport of the active ionic species (e.g. Li+ ions in a lithium battery). Second, it must wet and continually contact the electrodes and separator to be able to effectively transport the active ions. Third, the electrolyte should not leak, combust, or vaporize during cell storage or operation. Finally, it must be stable in the operating voltage range for the battery. These properties should be preserved over many cycles to ensure safety and proper battery operation. A key understanding of these essential features will guide the choice of components to use in the electrolyte solution.

Choice electrolytes for lithium metal batteries have promising properties for preventing dendritic short circuit, with the end goal to prevent the dendrite growth entirely or to delay its growth to the opposite electrode infinitely. All electrolytes are currently researched fall under one of two umbrella categories: solid state electrolytes and liquid electrolytes, or a combination of the two. Solid state electrolytes utilize the high moduli of polymer based systems in order to physically prevent dendritic growth. However, polymers yield low conductivity and have the so-called "Adhesion Dilemma", where the lithium metal anode recedes during battery operation and over time becomes detached from the polymer electrolyte, and creating large interfacial resistances.[15] Current research into liquid electrolytes is concentrated on room temperature ionic liquids, where salts characterized by an organic cation and a large, charge-delocalized anion are used in the electrolyte to facilitate ion movement. These ionic liquids are attractive due to their thermal and chemical stabilities, negligible vapor pressures, non-flammability, and low melting points. Ionic liquids have been used in electrodeposition, catalysis, energy, lubrication, bioscience,[30-33] and with the aforementioned properties, are promising for use as electrolytes in lithium battery applications. Unfortunately, for lithium battery applications, ionic liquids also suffer from low Li transference numbers (for pyrrolidinium and imidazolium Li transference numbers under 0.2 are typical) and low strengths.[34-36]

1.3 Piperidinium Based Ionic Liquids

Among room temperature ionic liquids, piperidinium based ionic liquids have come to light as one of the potentially viable ionic liquids for use in lithium battery applications. Studies in lithium-ion batteries have shown that a piperidinium based ionic liquid with 10 wt% vinylene

carbonate was able to maintain 90% of its initial capacity after 100 cycles.[18] Piperidinium ionic liquids paired with a charge delocalized bis(trifluoromethylsulfonyl)imide anion, or TFSI, anion have electrochemical stabilities of around 6V, as compared to others, such as ionic liquids based on imidazolium with stabilities of 4.3V vs lithium electrode.[19,20] 1-Methyl-1-propylpiperidinium paired with a TFSI anion(PP13-TFSI) has displayed conductivities around 1.51 mS cm^{-1} and a higher Coulombic efficiency than the equivalent pyrrolidinium based ionic liquids (P13-TFSI) when cycled in a Li/LiTFSI and IL-TFSI/$LiCoO_2$ cell.[21] Liu et. al. demonstrated that the addition of 1.44 moles of PP13-TFSI into their system of 1 mol of PEO_{18}LiTFSI was able to lower the interfacial resistance of the Solid Electrolyte Interphase (SEI) layer by up to a factor of 5**.** It was found that the lowering of interfacial resistances in lithium metal batteries effectively lowers the overpotential required for lithium plating and stripping and allows lithium to plate more evenly on the lithium anode.[6]

1.4 SEI layer

In batteries, it is known that upon cycling, a passivation layer known as the Solid Electrolyte Interphase forms on the electrodes. Spectroscopic investigations showed that the SEI layer in lithium ion batteries is composed of the electrolyte and its degradation products which have reacted with the lithium anode.[16] Once this layer forms, it is able to prevent further reaction of the electrolyte with the lithium while still maintaining pathways for Li^+ ions to navigate. The SEI may be approximated by an inorganic layer on the anode surface and a second porous organic layer formed over that, both layers of total thickness ranging from 2nm to tens of nanometers.**[17]** Much of the formation of the SEI occurs during the initial charge/discharge cycle

of battery operation. The majority of the interfacial resistance in lithium metal batteries is derived from SEI layer, with a small portion produced by the charge transfer resistance of the $Li^+ + e^- = Li$ reaction.[6]

1.5 Role of Silica Nanoparticles

Silica nanoparticles in the electrolyte solution play two important roles. First, it is able to lower the SEI layer resistance. Liu et. al. found that the addition of 10 wt% silica nanoparticles reduced the interfacial resistance of a Li/PEO_{18}LiTFSI electrolyte/Li symmetric cell by more than a fifth of its original value if left for 24 days (from 451.7 Ωcm^2 to 98.6 Ωcm^2), more than halving it initially (248.5 Ωcm^2 to 107 Ωcm^2).[22,29] The interfacial resistance consists of two components: the resistance of the passivation layer, in this case the SEI layer, and the charge-transfer resistance from the reaction resulting in metallic lithium ionization. A lower interfacial resistance is known to lower the overpotential of lithium plating/stripping and facilitates smooth lithium deposition. The authors also found that adding silica nanoparticles increased the short circuit time of symmetric cells run at at 0.5 mA cm^{-2} from 20h to 42h. Second, the mechanically rigid particles are able to act as junction points that are integral to the jammed structure created by a NOHMs material, which provides mechanical suppression of dendrite growth. This is explained in the next section.

1.6 NOHMs

Nanoscale organic hybrid materials (NOHMs) are a class of materials characterized by an inorganic core functionalized with an organic corona self-suspended in the organic material. These materials exhibit liquid like properties and are able to preserve their nanostructures even in the liquid state. They are versatile in that they allow manufacturing of materials with tunable properties by varying parameters such as the type of organic chain and inorganic core, particle loading, core size, corona length, suspension medium, just to name a few.[23] The range of properties shown in these materials varies from solids, stiff waxes, and gels to freely flowing fluids depending on the properties altered.

The nature of these materials allows particles in suspension to enter into the jammed phase transition. The inorganic cores act as junction points for the network structure providing mechanical strength to the system. At a certain threshold particle loading that is unique to each NOHMs system, the electrolyte become concentrated enough that the particles tethered with the organic corona are able to become coordinated with one another. When high enough concentrations are reached, the particles jam and create "cages" around one another, constructing a network where the particles are no longer able to freely explore phase space. These "cages" are associated with an energy threshold that must be overcome in order to rearrange the material. In the case of lithium metal batteries, the developing dendrites must then produce a stress high enough to overcome this energy barrier in order to propagate. Ueno et. al. reported that IL-based silica nanocomposite gels can exhibit MPa-scale elastic moduli.[24, 25]

1.7 Lithium Dendrite Growth Models

1.7.1 Chazalviel's Model

Chazalviel et al. created a dendritic growth model through a simple balancing of electromigration and diffusion terms. Their model illustrated the formation of a space charge region when the concentration of anions fell to zero in the vicinity of the lithium electrode. This region of anion depletion forms during charging when cycling at high current density which triggers uneven lithium deposition on the lithium electrode and ultimately leading to lithium dendrite. In a lithium battery, the anions in an electrolyte migrate oppositely of the lithium ions during a charge or discharge cycle to prevent the formation of an electric field. During a charge cycle, the anions migrate towards the cathode, forming a buildup of anions near the cathode, while the Li^+ ions are replated onto the lithium metal surface. In other words, while the lithium ions have a source and a sink, the anions have neither. When a threshold current density is reached, anions are no longer provided sufficient time to diffuse back to avoid space charge formation. According to Chazalviel et al., the depletion of the anions near the lithium metal anode forms a space charge region, a region associated with a large electric field and a large overpotential for lithium plating and stripping. They also found that the velocity of this dendrite growth must closely match the anion drift velocity to prevent the space charge from further increasing.[10,11] The space charge region forms at a time known as the "Sand's time" governed by the equation:

$$\tau = \pi D \left(\frac{C_0 e}{2 J t_a} \right)^2$$

According to this equation, there are two viable ways to prevent the formation of a space charge region: single ion conductors or use of a supporting electrolyte. A single ion conductor utilizes fixed anions (a t_a of 0, causing the sand's time to be infinite), allowing only Li^+ ions to transport through the electrolyte. A supporting electrolyte on the other hand allows both anion and cation movement, but is able to resupply anions to the area near the anode at a rate that matches that of anion depletion for a given period of time, delaying and possibly preventing formation of the space charge.

Since the potential evolution of a cell at a low and high current densities are vastly different, it was necessary for Chazalviel and his coworkers to define a crossover between the high and low current density regimes. When the concentration falls to zero near the anode, the space charge region forms, denoting a high current density regime. The concentration profile here followed:

$$\frac{\partial C}{\partial x}(x=0) = \frac{-J}{eD\left(1+\frac{\mu_c}{\mu_a}\right)}$$

and if $\frac{\partial C}{\partial x} < 2C_0/L$ where C_0 is the initial concentration and L is the interelectrode distance, then the concentration profile will evolve to a steady state, whereas if $\frac{\partial C}{\partial x} > 2C_0/L$ the concentration will go to zero at the negative electrode and the potential of the cell will diverge. Rearranging this equation they are able to come up with the equation for J*, the crossover value from a low to high current density regime:

$$J^* = \frac{2eC_0D}{t_aL}$$

For the low current density regime, anions are able to diffuse to the region near the cathode quick enough to prevent the formation of the space charge. In this regime, however, dendrites are still observed**.** In the low current density regime, Chazalviel et al. predict that local inhomogeneities derived from either the electrode surface or the passivation layer are responsible for dendrite formation that still form at a time very close to the predicted Sand's time[11].

1.7.2 Monroe and Newman's Model

Monroe and Newman simulated dendrite growth in a oxymethylene linked poly(ethylene oxide) (PEMO)-LiTFSI system at 85 °C in a cell with infinite x and z dimensions and setting the interelectrode distance in the y dimension to 100 μm, with a diffusion constant (D) of 5 x 10^{-12} m^2/s and a cation transference number (t^0_+) of 0.3. They were able to create a concentration, potential, and dendritic growth equations and consolidated them to form the model.

For the concentration profile, diffusion was accounted for via Fick's second law and a few set boundary conditions. Monroe et. al. assumed that the current evolved linearly with concentration at each point in the cell, the bulk concentration was always the average concentration of the cell, and the initial concentration was equal to the bulk concentration. The authors then non-dimensionalized length, the diffusion constant, and the current in order to be able to apply the model to a battery cell of any size, given that the x and z distance are large compared to the interelectrode distance. Utilizing Fourier series to split the non-dimensionalized current into a steady state and transient term

$$\theta(\xi,\tau) = \theta_{SS}(\xi) + \theta_T(\xi,\tau)$$

and reintegrating the transient non-dimensionalized current back into the boundary conditions to create the new boundary conditions, they were ultimately able to come up with an equation

$$\theta = -\xi + \frac{1}{2} - 4\sum_{k=1}^{\infty} \frac{1}{(2k-1)^2\pi^2} e^{-(2k-1)^2\pi^2\tau} \times \cos[(2k-1)\pi\xi]$$

that is able to give the concentration of the lithium salt at any time and position in the cell.

Calculations for the potential profile assumed a Butler-Volmer type expression that was used for the reaction kinetics, giving the equation

$$\frac{i}{F} = k_a \exp\left(\frac{\alpha_a F}{RT}\Phi\right) - k_c c \exp\left(\frac{-\alpha_c F}{RT}\Phi\right)$$

Where i is the current, k_a and k_c are the anodic and cathodic rate constants, c is the concentration of the salt, and α_a and α_c are transfer coefficients. They assumed that the potential in the solution relative to the cathode could be expressed as a sum of the open-circuit potential (OCP) and a surface overpotential:

$$\Phi = V_0 + \eta_s$$

When the current is zero, the OCP is reached. Assuming Butler-Volmer reaction kinetics, they were able to come up with an equation for the surface overpotential

$$\eta_s = \frac{2RT}{F}\sinh^{-1}\left[\frac{1}{2}\left(\frac{i}{i_{0,\mathrm{ref}}}\right)\left(\frac{c_{\mathrm{ref}}}{c}\right)^{1/2}\right]$$

and ultimately an equation for the instantaneous potential at any point across the cell.

$$\Phi_3(y,t) = \eta_s - \frac{i}{\Lambda}\int_0^y \frac{1}{c}dy + \frac{RT}{F}(1 - 2t_+^0)\ln\left[\frac{c(y,t)}{c(0,t)}\right]$$

Monroe and Newman assumed the conductivity of the separator to be linear in concentration. Solving this instantaneous potential equation as a function of time, current, position, temperature, bulk concentration of the lithium salt, and interelectrode distance, they were able to determine the evolution of the potential profile over time. In the simulation, the authors used values of D and t^0_+ previously stated, an initial reference current ($i_{0,ref}$) 3 mA/cm^2, and a reference concentration (c_{ref}) of 1 M.

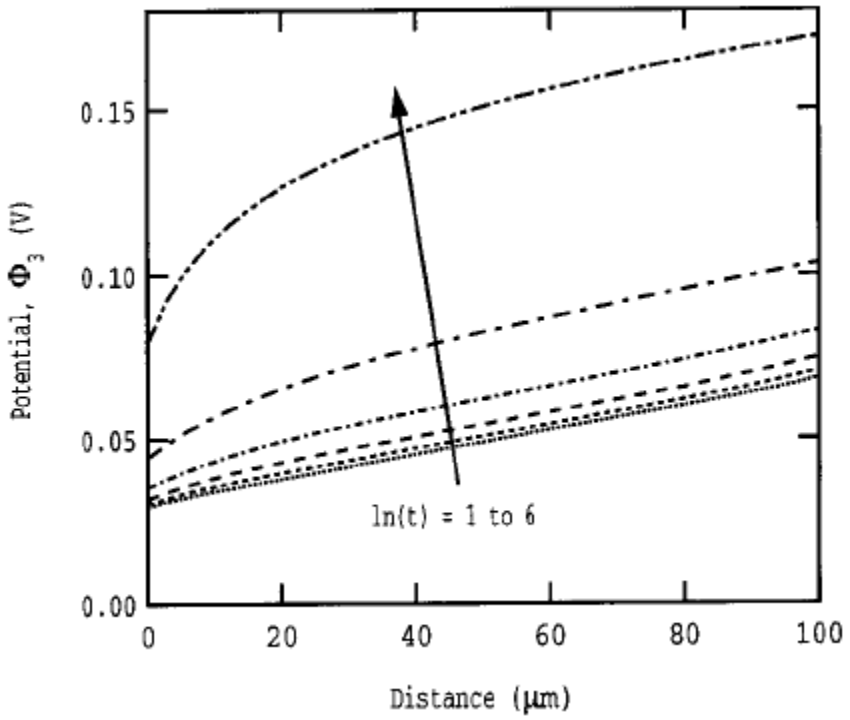

Potential profile obtained from Monroe and Newman's simulations

Zero distance represents the position of the cathode which has a potential of zero. It can be seen from the graph that the potential rises immediately to 0.4V upon application of a current and that the voltage only increases over time. This should be expected of real systems as well.

Dendritic growth rate calculations assumed that there existed only a single dendrite or that the dendrites were far enough apart that they did not affect each other. Monroe et. al. also assumed that dendritic growth did not affect the overall concentration and potential profiles. Using the theory of liquid droplets, the authors determined that surface forces at the dendrite tip causes pressure inside of the dendrite to increase as its radii of curvature (r_1 and r_2) decreases. Then, assuming that the dendrite tip is hemispherical, the two principle radii are the same and the pressure term becomes:

$$\Delta p = \gamma\left(\frac{1}{r_1} + \frac{1}{r_2}\right) = \frac{2\gamma}{r}$$

Since the cell is isothermal, they were able to relate the pressure difference to the chemical potential difference of planar lithium to curved lithium through the equation:

$$\Delta\mu = V\Delta p = \frac{2\gamma V}{r}$$

where V is the molar volume of solid lithium which is assumed to be the same as that in the dendrite and the electrode.

In developing an equation to determine the kinetics of the dendrite growth, Monroe and Newman again assumed a Butler-Volmer type equation. The authors separated the area surrounding the dendrite into three regions: inside the dendrite (α'), at the tip surface (δ), and in the vicinity of the tip (δ'). Taking into account the concentration, chemical potential, activity of lithium in these regions, the effect of the lithium curvature in the dendrite, and eliminating the concentration at the dendrite tip, they were able to come up with the equation for the current density normal to the hemispherical dendrite tip:

$$\frac{i_n}{i_{0,\mathrm{ref}}} = \frac{\exp\left(\frac{2\gamma V}{rRT}\right)\exp\left(\frac{\alpha_a F\eta}{RT}\right) - \exp\left(\frac{-\alpha_c F\eta}{RT}\right)}{\left(\frac{c_{\mathrm{ref}}}{c_{\mathrm{Li}^+}^{\delta'}}\right)^{\alpha_a} + \frac{(1-t_+^0)ri_{0,\mathrm{ref}}}{FDc_{\mathrm{Li}^+}^{\delta'}}\exp\left(\frac{-\alpha_c F\eta}{RT}\right)}$$

When accounting for the three profiles previously discussed (concentration, potential, and dendrite growth), the results from simulations of their model illuminated many important aspects of cell performance to consider. First, the authors found that the dendrite growth rate increases as it propagates across the cell. This is due to the increased current density through the dendrite tip as the dendrite grows across the cell. A depletion region follows the dendrite tip as it propagates through the cell, and the concentration gradient increases between this region and the concentration of the cell at the dendrite position as the dendrite grows. This produces an augmented electric field that forces lithium to deposit quicker to prevent the depletion region from further increasing, and in turn, the current density through the tip is increased. Second, the authors found that lowering the current density prolonged the time to short circuit. The simulation suggested that running the battery above 75% of the limiting current produced a short circuit in less time than required for a single 3h charge cycle. Third, running the simulation to determine the effect of gap width demonstrated that larger interelectrode distances allowed for longer short circuit times, but the benefits from this displayed diminishing returns as the gap width increased. This is due to the acceleration of the dendrite growth velocity as potential increases,

$$v_{tip} = \frac{i_n(c,\eta)V}{F}$$

and the potential evolution rate is increased as the distance of dendrite growth increases, causing the dendrite to grow over the added gap quickly. Finally, it was found that an increase in the value of the diffusion constant or an increase in the cation transference number both increased the charged passed before short circuit. The maximum in the data the data suggests that there exists an optimal t^+ and D that should be sought after.

In another paper by Monroe and Newman, they expand on this model by including mechanical forces in the simulation. They discover that the total stability parameter, which consists of a surface tension, deformation forces, and compressive forces, produces a negative value when the electrolyte shear modulus is twice that of the lithium electrode (approximately 7 GPa) , corresponding to stable electrodeposition.[27] This model assumed that perturbations across the lithium electrode surface produced seeds for dendrite formation. The surface force across the electrode/electrolyte interface was found to increase linearly with the displacement frequency, implying that an increase in the displacement frequency decreases the "valley to valley" distance across electrode protrusions. This work used a displacement frequency of $2\pi/0.1$ μm. From this model they were able to deduce that hard particulate additives decrease the bulk compressibility of a polymer electrolyte, which is what leads to longer initiation times for dendritic deposits.

1.7.3 Balsara's Novel Idea

Balsara et. al. followed up on Monroe and Newman's work, running lithium symmetric cells in an unconventional cycling test as opposed to the common polarization tests. Each cell

contained a polystyrene-block-polyethylene oxide block copolymer electrolyte (SEO) or a polyethylene oxide homopolymer electrolyte (PEO). Each cell was run in the current density range of 0.04 – 0.256 mA/cm^2 with a three hour half cycle time. The charge passed before the dendrite short (C_d) was recorded for these cells once the short was observed. In one of the runs, Balsara and his coworkers found that the SEO cells ran at 0.17 mA/cm^2 had an order of magnitude increase in C_d over its PEO counterparts at a fixed modulus, showing that the modulus is not solely responsible for preventing dendrite growth[15]. Furthermore, Balsara and his coworkers plotted inverse C_d vs the storage modulus in their SEO electrolytes and tentatively found a linear relationship. Assuming this relationship is correct, a value of 0 for the inverse of C_d would correspond to an infinite charge passed before short circuit, or more concisely, no short circuit would ever form. For the SEO system, the storage modulus required for this was 10.2 GPa with ±1.2 GPa error. Other systems where other factors may come into play could require a lower storage modulus to achieve the same goal.

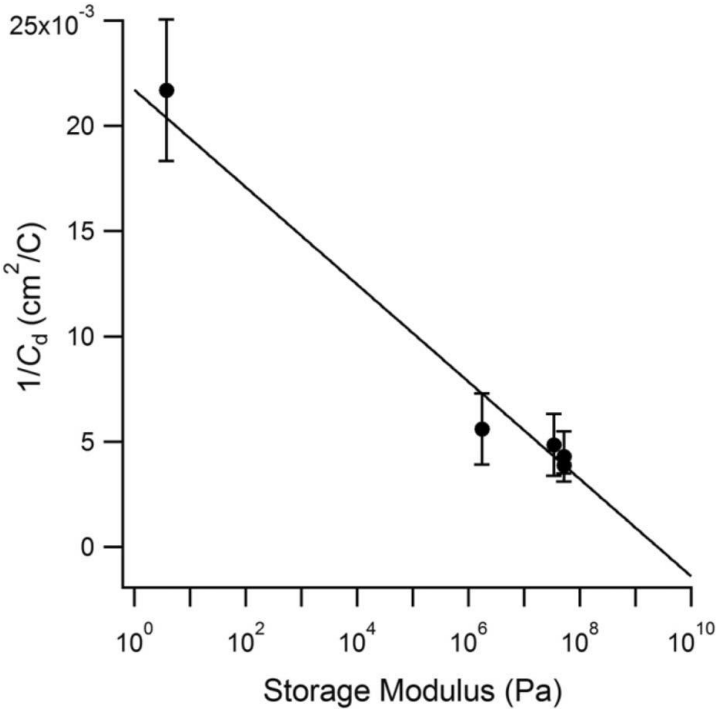

CHAPTER 2

METHODS

2.1 Synthesis of SiO_2-PP-TFSI

1-methyl piperdine and 3-chloropropyl trimethoxysilane, commercially available from Sigma-Aldrich, were dissolved in DMF in a 1 : 1.2 molar ratio and stirred in a sealed environment at 80°C for 2 days. The reaction product was washed with ether 3 – 4 times to remove any unreacted materials and impurities. The ether was evaporated off the remaining product to obtain the 1-methyl-1-propyl piperidinium chloride with the trimethoxysilane tail. The 1-methyl-1-propyl piperidinium chloride with the silane tail was reacted with SM30 LUDOX, 30% 7 nm silica nanoparticles by weight in aqueous suspension, in a 1: 2.2 weight ratio in deionized water at 95 °C for 12 hours. Approximately 2mL of hydrochloric acid was added to the solution to bring the pH down to 2 in order to facilitate leaving of hydroxyl groups on the silica surface and attachment of the silane group. The 1-methyl-1-propyl piperidinium chloride with the silane tail was added in two equal steps throughout the reaction, once initially and once 6 hours into the synthesis. The resultant product was then washed with a 50/50 methanol/ether cosolvent to allow the nanoparticles to fall out of solution. The piperidinium functionalized nanoparticles and solvent were centrifuged at 8000 rpm for 20 minutes to separate solvent, unreacted materials, and ionic liquid-functionalized nanoparticles. Top layer of excess solvent and unreacted materials was removed and the IL-functionalized nanoparticles were lyophilized in a freeze dryer to allow the remaining traces of solvent to evaporate, leaving only the chlorinated tethered particle (SiO_2-PP-Cl) as the product. Equivalent weights of the SiO_2-PP-Cl product and LiTFSI were dissolved separately in deionized water and the LiTFSI / DI water

solution was added to the SiO_2-PP-Cl solution with continuous stirring. An immediate reaction was observed and due to the hydrophobic nature of the TFSI anion, the final tethered particle (SiO_2-PP-TFSI) product precipitated out of solution. The tethered particle was separated from water through centrifugation and freeze dried to evaporate residual water and to obtain the pure tethered particle powder. A schematic is shown in Figure 1 to illustrate the synthesis steps.

To make the final electrolyte solutions, a predetermined amount of tethered particle powder was redissolved in acetone and stirred for 1 day to achieve a fully dissolved solution. A calculated 1M LiTFSI and different proportions of PC were then added to the dissolved SiO_2-PP-TFSI to create the final electrolyte of several different particle loadings.

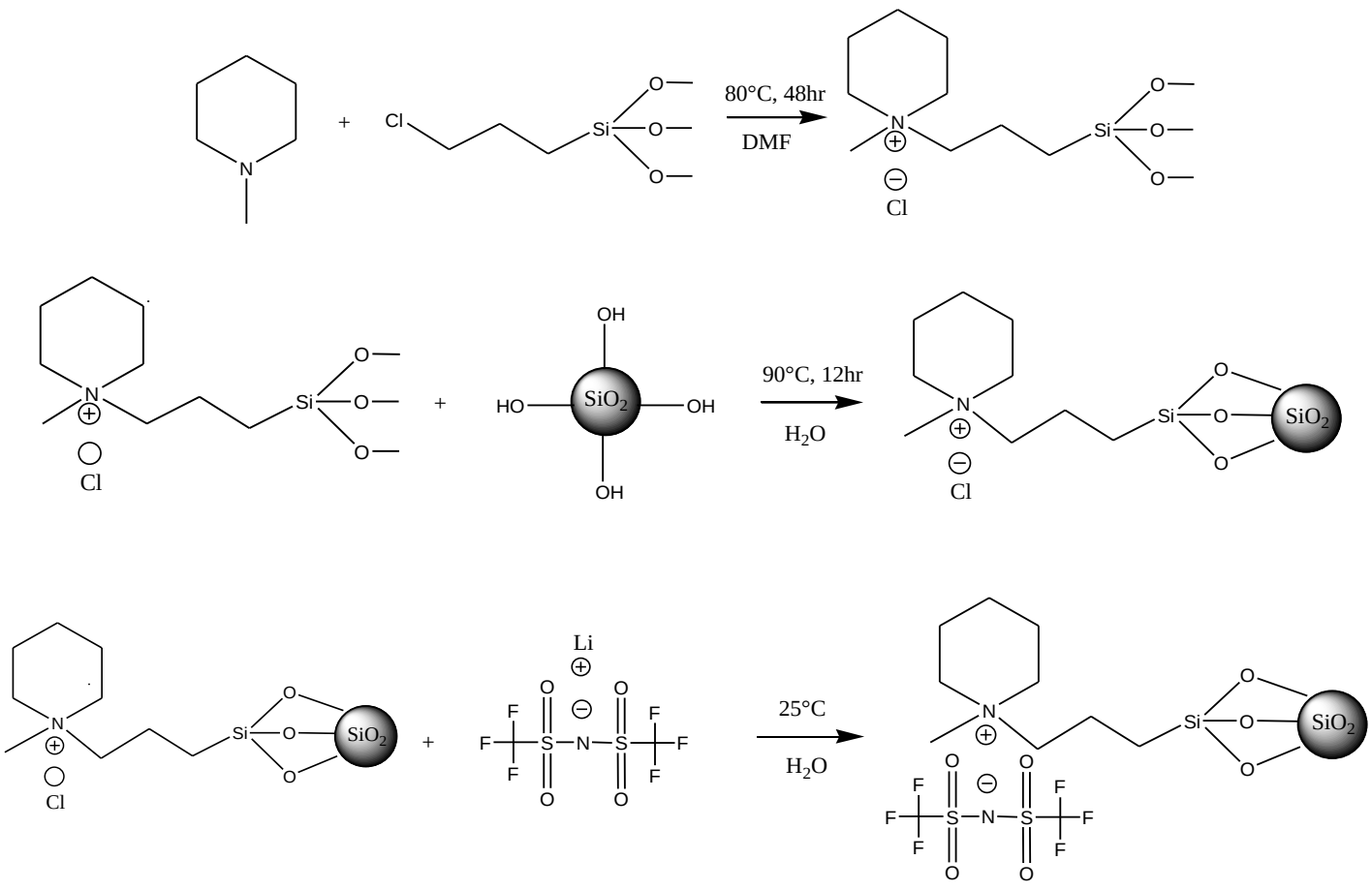

Figure 1

2.2 Calculation of 1M LiTFSI

1M LiTFSI was calculated only against the PC added to each electrolyte loading. Although the silica cores contribute to the volume in solution, they are solid particles and do not act as a solvent to the LiTFSI. Using 1.205 g/cm^3 for the density of PC and 287.07 for the molecular weight of LiTFSI, the weight fraction of LiTFSI to PC was found to be 0.238 : 1 to achieve 1M LiTFSI. It was assumed that the TFSI anions paired with the piperidinium cations off of the tethered particles did not significantly contribute to the overall concentration of the TFSI in the electrolyte.

2.3 Calculation of Volumetric Particle Loadings for Tethered Electrolyte

Volumetric loadings of the particles were calculated for a range of electrolytes that exhibited liquid to solid-like properties. The calculations assumed that only the PC solvent and the silica nanoparticle cores of the tethered particles contributed to the volume of the overall electrolyte. Molar volume contributions of the piperidinium chains and the LiTFSI were not accounted for. The density of the silica cores was taken to be 1.8 g/cm^3 and the density of PC was 1.205 g/cm^3. From Figure 2, it can be seen that for every 1 g of the tethered particle, 0.795 g of that weight is derived from the silica nanoparticle core. Using the silica density, it was calculated that 0.795 g of silica translated to 0.442 cm^3 of volume. Dividing this by the total volume (part of which contained the unknown volume of PC) and setting that equal to the volumetric particle loading desired, the volume of PC was able to be worked out. The volume of PC found was then converted into grams using the density of PC and thus a weight ratio of PC to

tethered particle was found. Table 1 shows those ratios extrapolated to yield a 10 g amount of the tethered electrolyte.

Φ (Particle loading)	PC (g)	Tethered Particle (g)	LiTFSI (g)
0.11	6.82	1.56	1.62
0.23	5.59	3.08	1.33
0.36	4.39	4.56	1.05
0.38	4.19	4.82	1.00
0.41	3.92	5.14	0.93
0.44	3.68	5.44	0.88
0.48	3.37	5.83	0.81
0.53	2.98	6.31	0.71

Table 1

*For 10g amounts

2.4 Calculations of Equivalent Particle Loadings for Control Electrolytes

The control electrolyte was calculated based on the grafting density of the tethered particles. In Figure 2 it is seen that 20.5 wt% of the tethered particle is comprised of piperidinium TFSI chains with the silane tail. Piperidinium TFSI was ordered from Ionic Liquid Technologies, but this ionic liquid did not have the silane tail. To find the appropriate amounts of ionic liquid to use in the control electrolyte, it was necessary to find the molar ratio of the piperidinium TFSI chains with the silane tail to the piperidinium TFSI without the silane tail. This ratio was found to be 0.85. 20.5% of the third column in Table 1 was taken and multiplied

by 0.85 to find the weight of the piperidinium TFSI to be added to equivalent amounts of PC and LiTFSI.

Φ (Equivalent particle loading)	**PC (g)**	**Piperidinium TFSI (g)**	**LiTFSI (g)**
0.11	6.82	0.272	1.62
0.23	5.59	0.536	1.33
0.36	4.39	0.794	1.05
0.38	4.19	0.839	1.00
0.41	3.92	0.874	0.93
0.44	3.68	0.947	0.88
0.48	3.37	1.015	0.81
0.53	2.98	1.099	0.71

Table 2

2.5 Calculation of Grafting Density

Grafting density of the piperidinium with the silane tail to the silica nanoparticle was calculated using TGA data of the tethered particles without the PC and 1M LiTFSI. This calculation assumed that each piperinidium cation was paired with its own TFSI anion, the chains degraded or burned off completely when undergoing TGA, and the silica nanoparticles are 7 nm in diameter and have a density of 1.8 g/cm^2. The molecular weight of the piperidinium chains with the associated TFSI was found to be 496.41 g/mol. Using the results in Figure 4, it was determined that 20.5 wt% of the powder was comprised of the piperidinium TFSI chains and

through a calculation of the surface area of the nanoparticles and the number of chains in the sample, it was found that the grafting density is 0.657 chains/nm^2.

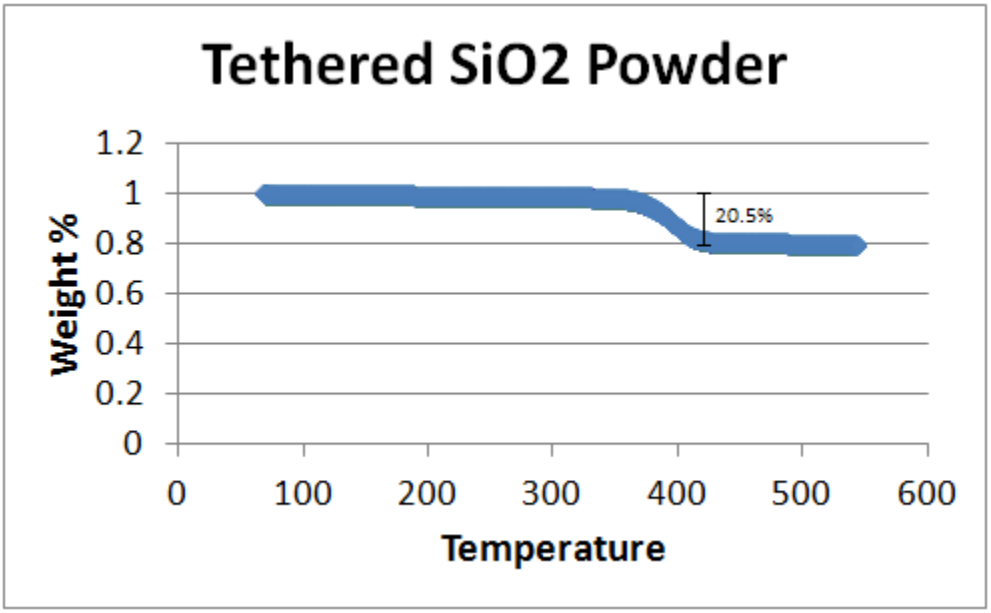

Figure 2

2.6 Analysis Methods

Thermal stability measurements were taken using a TA instrument DSC Q-2000 in an aluminum Tzero pan and a TA instrument DSC Q-500 under nitrogen flow. The ionic conductivity of the systems were taken using a Novocontrol N40 broadband dielectric spectrometer. Rheology measurements were performed with a Paar Physica MCR 501 with 10mm and 25mm cone diameters with a tip angle of 1-4 degrees. NMR was performed in an INOVA 400 using VNMRJ 1.1B and VNMR 6.1C software. SEM images were taken using a LEO 1550-FESEM in conjunction with EDX to determine surface compositions of the SEI layer. Polarization experiments and cycling experiments were performed using symmetric and full cell

batteries with Li/tethered electrolyte/Li and LTO/glass fiber + tethered electrolyte/Li setups, respectively, in a battery cycler**.** All cells were made in a argon filled glovebox with oxygen and water levels below 10 ppm.

CHAPTER 3

RESULTS

3.1 NMR

Composition analysis of 1-methyl-1-propyl piperidinium chloride with the silane tail by proton NMR spectroscopy shows peaks in all the expected locations. The peaks are labeled accordingly in Figure 2 confirming that synthesis of the ionic liquid with the silane tail was successful. The large peak at around 1.1 ppm is derived from the CH_3 hydrogens of ethanol that was used as a cleaning solvent for the lab equipment used during the synthesis. However, the integration displayed is too large to be simply derived from residual ethanol. Immediately following this step in the synthesis, the product was washed several times with diethyl ether to remove any unreacted material from the product. It is possible that the cleaving of this diethyl ether resulted in the formation of ethanol. The small peaks from 2.1 ppm to 3.0 ppm were all solvents used during some point in the synthesis or NMR analysis. Acetone was simply used for cleaning lab equipment. DMSO was used as the solvent for NMR analysis and contained 99% NMR silent deuterium in place of hydrogens. However, the deuterated DMSO is very hygroscopic and readily exchanges protons with water when in solution, creating slightly more hydrogen in DMSO. The DMSO peak thus arises from the remaining 1% hydrogen in the solvent as well as the extra exchanged DMSO hydrogens. The remaining two small peaks are attributed to residual DMF solvent that was used in the synthesis of the 1-methyl-1-propyl piperdinium chloride with the silane tail. The peak at 3.2 is from the CH_3 of methanol created from the hydrolyzation of the methyl groups of h*, the * denoting different degrees of methylization. Under peaks c and d is buried the CH_3 peak of ethanol and the large peak displays peaks for

silane methyl groups as well as the deuterated water created by the exchange between DMSO and water. Finally, the OH group protons of methanol and ethanol are shown around 4.4 and 4.6 ppm, thus accounting for all peaks shown.

It is noteworthy that several peaks are affected by the different degrees of the methylization off of the methoxysilane group. The peaks labeled a, h*, and g in Figure 2a all display a step down of three different peak heights of varying chemical shifts that can be seen in Figures 2b and 2c. This suggests that there could be one, two, or three methyl groups off the silane tail. Since there are no peaks for an ionic liquid with zero methyl groups, it can be concluded that these were washed away during purification. Interestingly, the different degrees of methylization affecting the chemical shift of the methyl group labeled “g” indicates that this side of the ionic liquid could be folding back on itself, causing g to be much more affected by what is attached to the silane side than the illustration suggests.

a)

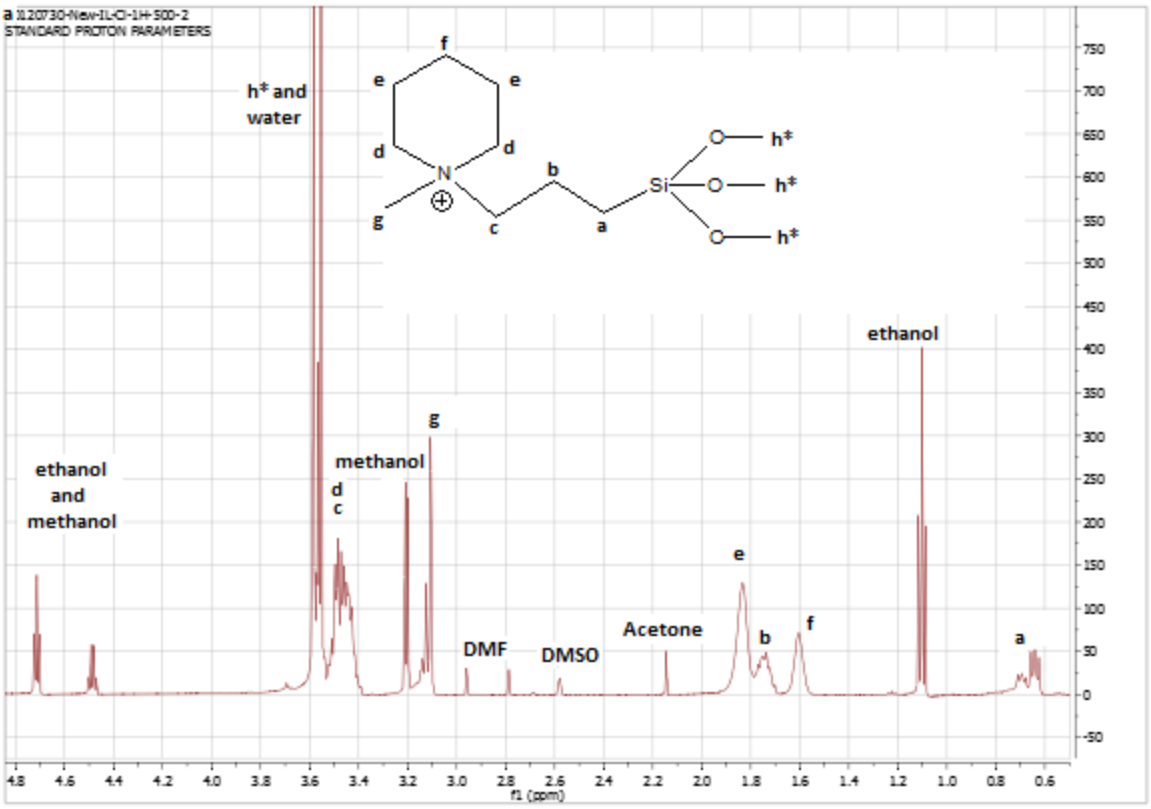
STANDARD PROTON PARAMETERS
h* and water
ethanol and methanol
methanol
ethanol
DMF
DMSO
Acetone
f1 (ppm)

b)

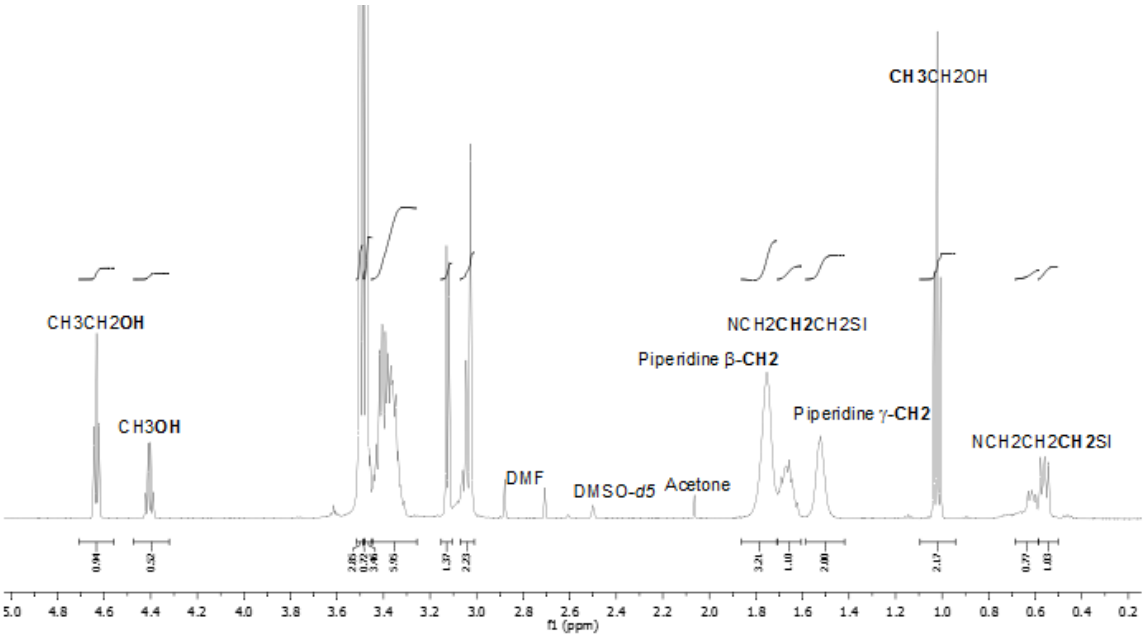
CH3CH2OH
CH3OH
DMF
DMSO-d5
Acetone
NCH2CH2CH2SI
Piperidine β-CH2
Piperidine γ-CH2
f1 (ppm)

c)

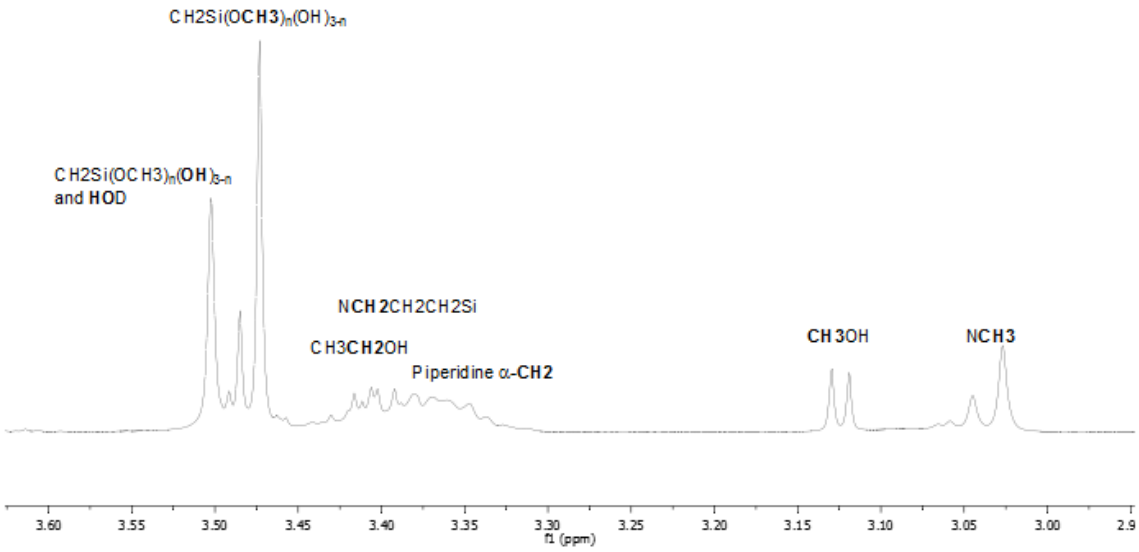

Figure 3

a) Peaks labeled corresponding to each proton NMR active group in the piperidinium ionic liquid

b) detailed labeling of peaks showing step down caused by different degrees of methylization of the silane tail

c) zoomed in detailed labeling of groups with chemical shifts between 2.9 and 3.6 ppm

3.2 Thermal Stability

TGA measurements reveal that the electrolyte is stable up to 80 °C, when the first component of the electrolyte, propylene carbonate, begins to vaporize. TGA was performed on pure PC for reference. An interesting observation in this data is that the PC does not vaporize at the same temperature for all particle loadings, implying that the tethered electrolyte imparts a stabilizing effect upon the PC. In this case, it seems that the tethered particles are able to effectively lower the volatility of PC. It can be seen that the 11% particle loading electrolyte solution begins to degrade around 80 °C whereas the 53% particle loading begins its degradation around 110 °C. The start of degradation here was said to be at the temperature which the electrolyte degraded 1% of its initial weight. This phenomenon, however, could be caused by

other unexpected occurrences that the electrolyte displays when heated. For instance, it is possible that a skin layer forms when the tethered electrolyte is heated. In some oils, the oil is able to form an elastic film after exposure to air due to oxidation of the organic compounds and subsequent cross-linking[7]. In the tethered electrolyte, it is possible that ionic crosslinking similarly forms a skin layer that shields the PC from evaporating or degrading. It is also possible that the tethered nanoparticles are able to shield heat from the PC by absorbing the heat more efficiently than PC would. The PC would then experience a lower temperature than the actual ambient temperature at a given heating rate. Further study is needed to fully understand the reason for this occurrence.

The second dip in the weight percent vs temperature data is when the silated ionic liquid ligands begin to degrade from the silica nanoparticle, occurring initially at 380 °C. Again TGA on the pure piperidinium TFSI was performed for reference. The temperature at which this happens is consistent across all particle loadings and it is noted that no stabilization is evident on the ionic liquid chains compared to that exhibited by the PC. At the end, all that is left at 550 °C are the silica nanoparticle cores.

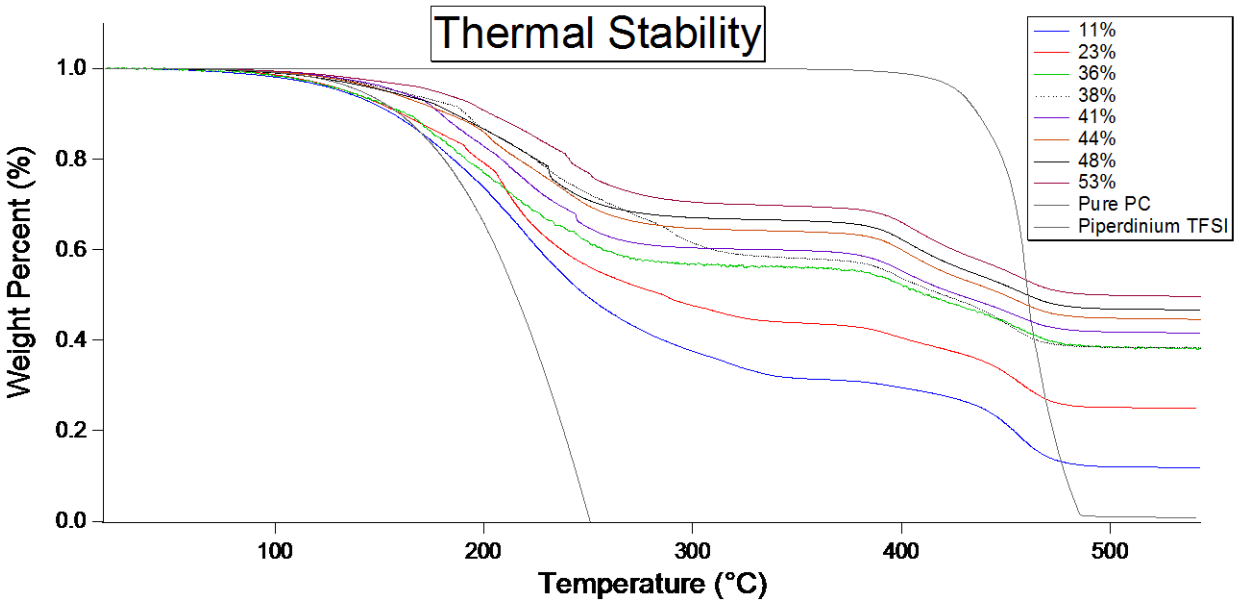

Figure 4

3.3 Impedance

Impedance was performed on uncycled lithium symmetric cells that were left for 2-3 days to show the benefits of the tethered electrolyte with PC and 1M LiTFSI on interfacial resistance against that of the equivalent free ionic liquid electrolyte. The impedance results show that the interfacial resistances of the tethered electrolyte with 11% (Figure 4) and 23% (Figure 5) particle loadings are lower than that of the free ionic liquid electrolyte by up to a factor of 4. The bulk resistance and the interfacial resistance can be well approximated by the first x-intercept of the semicircle and by the diameter of the semicircle, respectively. The tail after the semicircle is due to the contribution of diffusion of the ions in the electrolyte and is modeled by the Warburg diffusion coefficient. The impedance profiles were fit to a model open circuit to determine the resistances and diffusion coefficients.

While interfacial resistance is lowered in the 23% electrolyte solution, the bulk resistance is increased. The increased viscosity due to the silica nanoparticles closes off available ion conduction pathways, causing the lithium ions moving through the electrolyte to experience a higher resistance. Although this reduces the conductivity of the tethered electrolyte compared to the control electrolyte, it can be seen in the following section that this effect is small. The low loading of the 11% solution was not significantly affected by this increased viscosity.

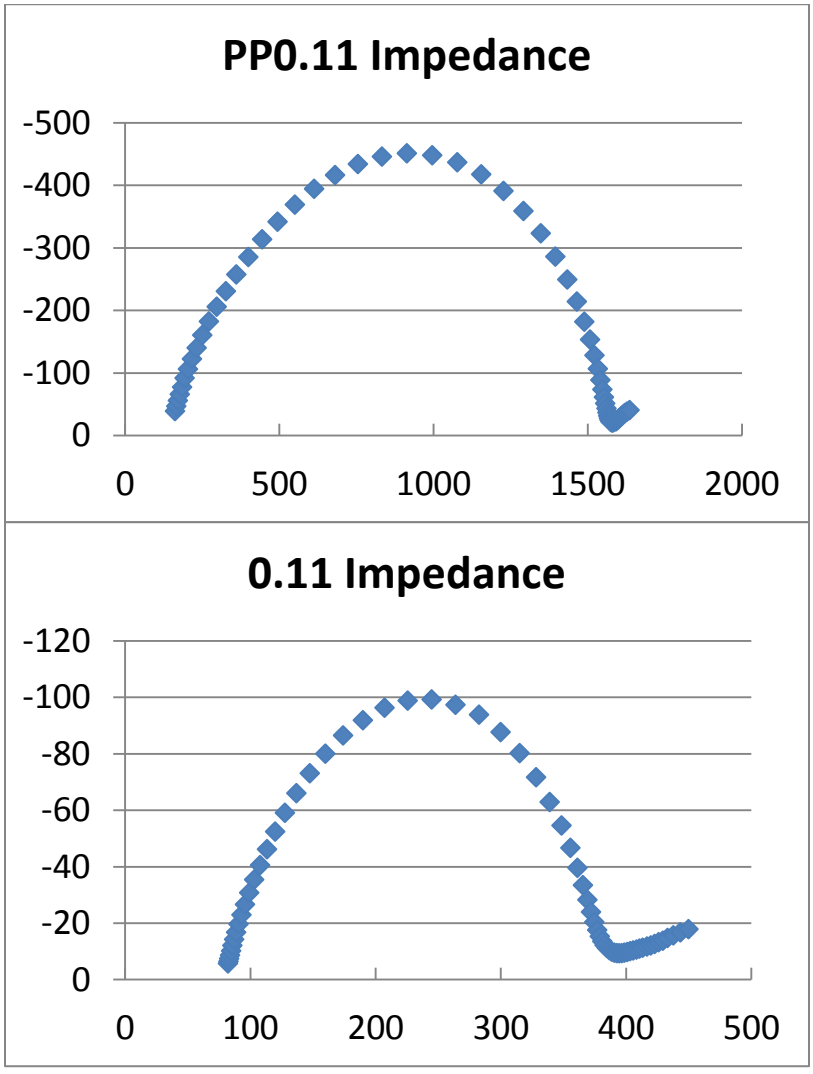

Figure 5

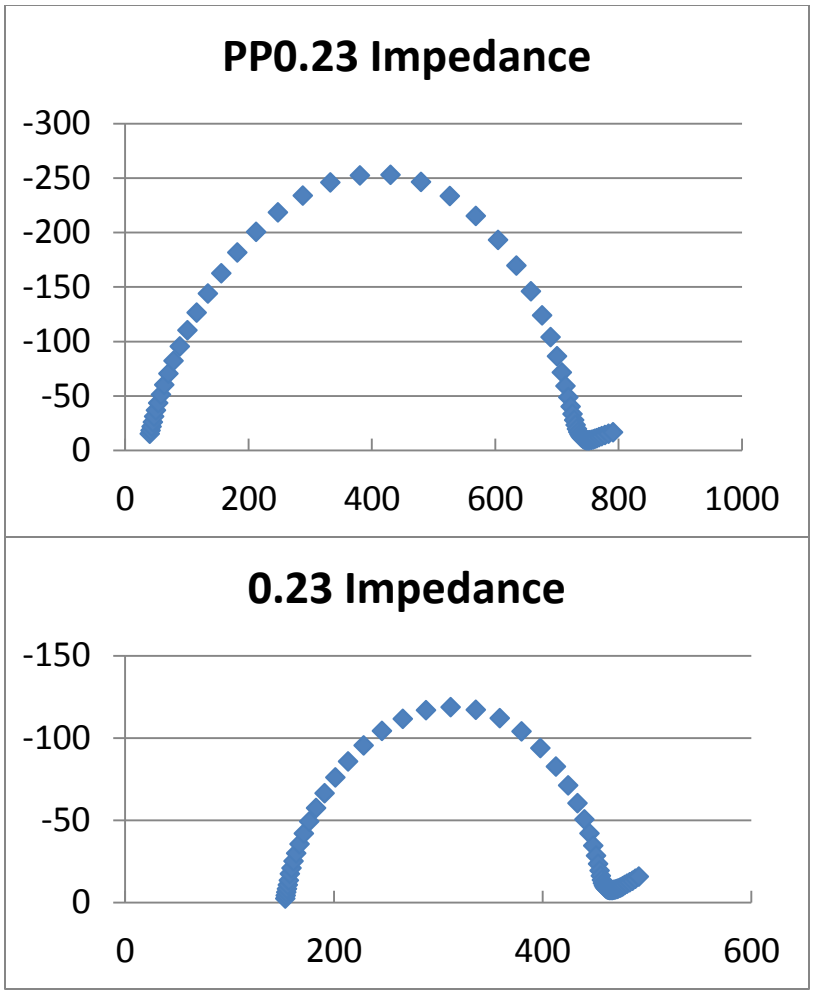

Figure 6

3.4 Conductivity

Conductivity measurements in Figure 7 show conductivities ranging from 6 x 10^{-4} to 5 x 10^{-3} mS/cm at room temperature that inversely correlate with particle loading. However, the highest particle loading material shows only a ten-fold decrease in conductivity while exhibiting over three orders of magnitude increase in storage moduli as shown in Figure 8a. This represents an uneven trade-off between conductivity and mechanical strength that can be manipulated to determine a particle loading that will maximize the benefits of mechanical dendrite suppression

and maintain the necessary conductivity for proper battery function. Also, it can be seen from the plot that the shape of each curve exhibits a more pronounced bend as the particle loading is increased, causing the data to become more spread out at lower temperatures. The fit curves are of the VFT form $\sigma = A \exp(-B/(T-T_0))$, where σ is conductivity, A is the pre-exponential factor, B represents the effective activation energy for coupled ions and local segmental motion, and T and T_0 are the measurement and reference temperatures, respectively. In this case the reference temperature was taken as the glass transition temperature obtained by DSC analysis. A VFT form that properly fits the data infers that the conductivity stems from local chain relaxation, segmental motion, and electrolyte crystallinity. The extra mobility of the chains that have one end free allows an exaggerated swinging motion that is able to aid ion movement through the electrolyte medium that has a more distinct impact on conductivity at lower temperatures. This swinging is related to the glass transition temperature and the swinging has a greater effect the higher the operating temperature is above the glass transition temperature. This causes the effect to be more pronounced at lower temperatures in the electrolytes with the lowest glass transition temperatures. At the highest temperatures, ionic motion is dominated more by the solvation sphere and transition state for ionic motion, which is more consistent across particle loadings, resulting in a more compact data set at higher temperatures.[13]

It can also be seen from the data that the addition of nanoparticles themselves insignificantly affects the conductivity, but rather the resultant increase in viscosity caused by these nanoparticles that reduces the conductivity. An increase in viscosity is known to cause a decrease in the hole free volume in the electrolyte and diminishes available pathways for ions to move through the electrolyte, ultimately resulting in a significant decrease in conductivity. Kim et. al. reported a pure 1-methyl-3-propylimidazolium TFSI ionic liquid with an ionic

conductivity of 7.42 x 10^{-3} S/cm at 30 °C dropped to 1.17 x 10^{-3} S/cm and a pure 1-methyl-1-butylpyrrolidinium TFSI dropped from 3.77 x 10^{-3} to 8.67 x 10^{-5} when the viscosity was increased by a 1:1 molar ratio addition of LiTFSI.[14] The conductivity of the nanoparticle-free control solution in Figure 7b shows that the conductivity is consistently high with minimal change in conductivity over a volumetric particle loading range from 11% to 48%. In addition, comparison of the 11% particle loading electrolyte to the control solution without the NOHMs (PC and 1M LiTFSI) shows an almost perfect overlap of the data, indicating that the nanoparticles themselves have no detrimental effect on the conductivity.

a)

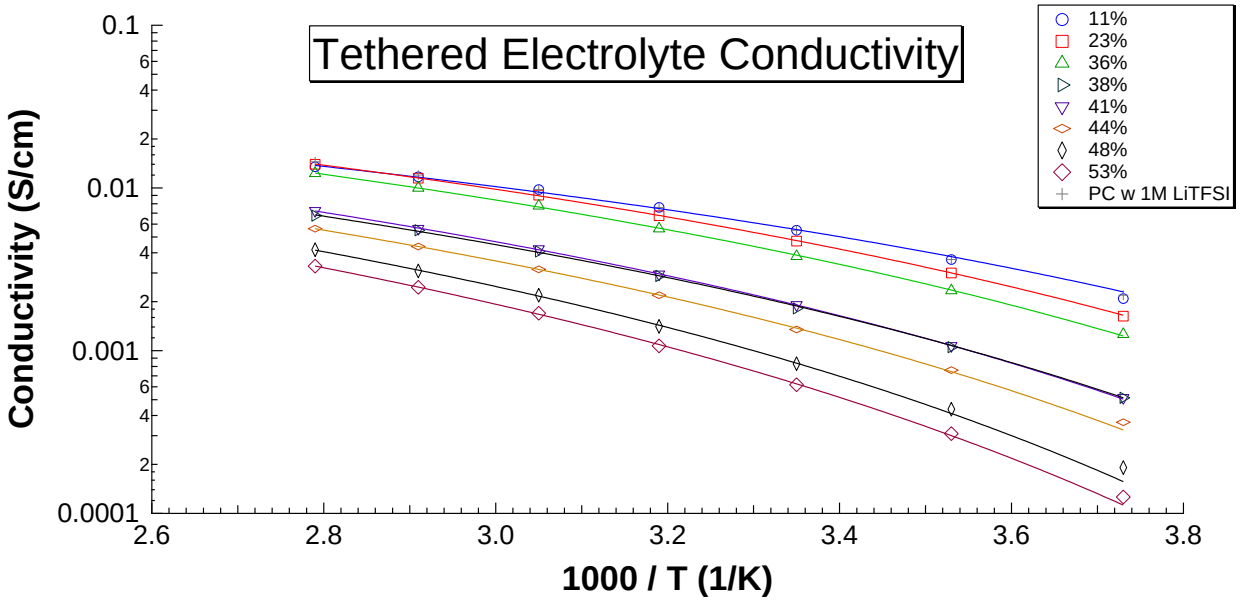

b)

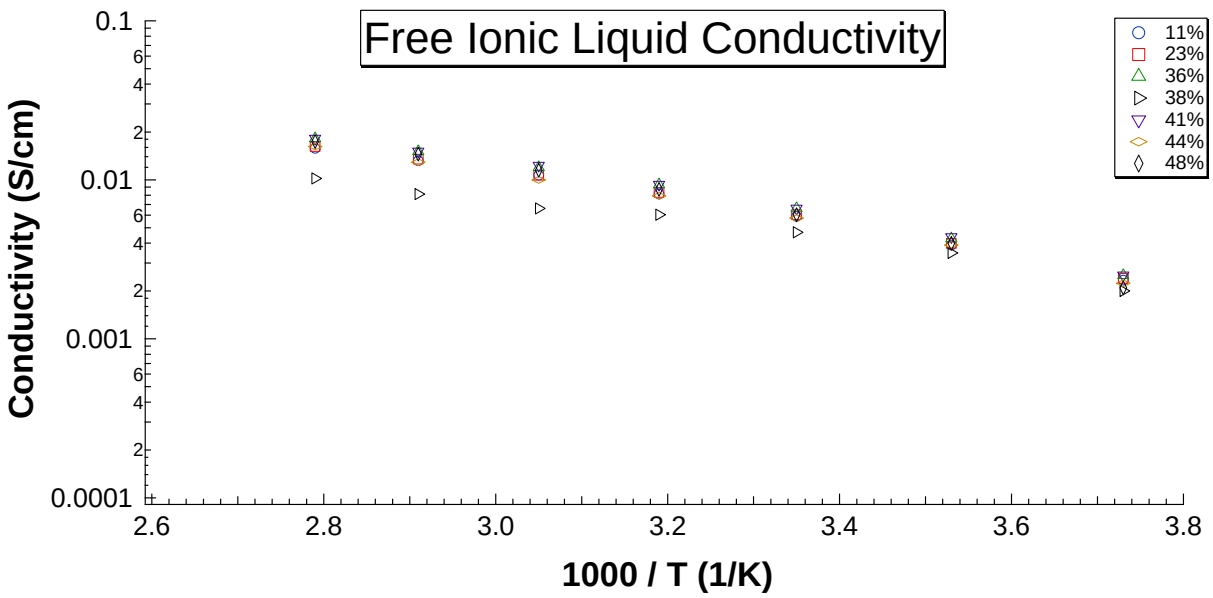

Figure 7

VFT Curve Parameters					
Loading	Chi Square	A	B	C	Tg
11	2.657e-07	0.873	-12.96	5.912	-104
23	1.076e-08	1.858	-15.08	5.877	-103
36	2.518e-08	2.02	-15.39	5.809	-101
38	1.943e-08	1.455	-15.48	5.677	-97
41	6.217e-09	1.96	-16.36	5.709	-98
44	2.359e-09	1.535	-15.66	5.582	-94
48	4.672e-09	1.724	-16.10	5.460	-90
53	1.435e-09	2.315	-18.09	5.551	-93

Table 3

3.5 Lithium Transference Number

The lithium transference number was calculated by the method formulated by Bruce and Scrosati. The lithium transference number represents the portion of the ionic conductivity that is

due to lithium transport, the active species in a lithium metal battery. According to Bruce and Scrosati's method:

$$T_{Li^+} = \frac{I_{ss}(\Delta V - I_0 R_0)}{I_0(\Delta V - I_{ss} R_{ss})}$$

where T_{Li}^+ is the lithium transference number, I_0 and I_{ss} are the initial and steady state currents of a cell undergoing a polarization potential of ΔV, and R_0 and R_{ss} are the interfacial charge transfer resistances before and after polarization. In this method, the cell resistance and current is measured before the cell is polarized to obtain reference points of the electrolyte as a whole. Theory then states that when the cell is completely polarized the TFSI anions are driven to one electrode while the lithium cations that have a source from which to strip and a sink to deposit are able to be transported freely to the opposite electrode. At steady state, only these lithium ions are contributing to the current of the cell.

Using this method, it was found that the piperidinium tethered electrolyte with 11% and 23% particle loadings have a T_{Li}^+ of 0.26 and 0.52 , respectively. These values are higher than expected since ionic liquids are known to be associated with low lithium transference numbers. Lithium transference numbers in the range of 0.1-0.25 are typical in NOHMs systems (0.2 for systems of imidazolium and pyrrolidinium based ionic liquids with TFSI as the counterion).[34-36] Further doubt is thrust upon these results when compared to those of an imidazolium NOHMs system, that exhibits a decreasing T_{Li}^+ as particle loading is increased.[12] However, these numbers are not out of the range of possibilities. Moganty et. al. reported an imidazolium - zirconia nanoparticle system that exhibited a lithium transference number of up to 0.35.[40] The jammed network of the electrolyte also provides an anchor to the covalently tethered piperidinium cation,

significantly lowering its contribution to ionic conductivity and in turn raising the contribution of the lithium cation to ionic conductivity. The lithium transference number is then dependent on two variables, the drop in overall conductivity due to increasing viscosity at higher particle loadings and the decrease in the piperidinium cation contribution to overall conduction. Since the conductivity of the piperidinium – silica nanoparticle system is less affected by an increasing viscosity than other ionic liquid NOHMs systems, it is reasonable to assume that an increasing T_{Li^+} with increasing particle loading is not out of the question. Further study is required for a concrete conclusion.

3.6 Rheological Studies

Rheology was performed in a Paar Physica MCR 501 with 10mm and 25mm cone diameters with a cone angle of 1-2 degrees. Under a dynamic or oscillatory loading, the shear modulus consist of two parts, the storage modulus that represents the portion of the material response that is in phase with the applied stress and the loss modulus, the portion which is out of phase. The storage modulus is related to the portion of the energy that is able to be recovered after deformation and the loss modulus is related to the energy that is lost as heat.

$$G = G' + iG''$$

Where G is the dynamic shear modulus, G' is the storage modulus, and G" is the loss modulus.

Results in Figure 6a and 6b show that almost all the particle loadings exhibit storage moduli greater than their loss moduli at low strains, implying that the material has a more solid-

like response to deformations. The hump exhibited in the loss modulus for higher particles loadings is characteristic of a jammed material. This hump occurs from the frictional loss that happens when the material becomes unjammed. Since the particles are forming cages around one another, the slipping of these particles causes frictional loss as heat and thus forms this hump before the material begins to flow. The hump begins to disappear around 41% and is completely absent at 36% loading. Towards higher strains, the material exhibits a trend characteristic of plastic flow where the loss modulus overtakes the storage modulus as the material begins to yield, showing a more liquid-like response at higher strains. The storage moduli here range from 10^6 to 10^3 Pa.

a)

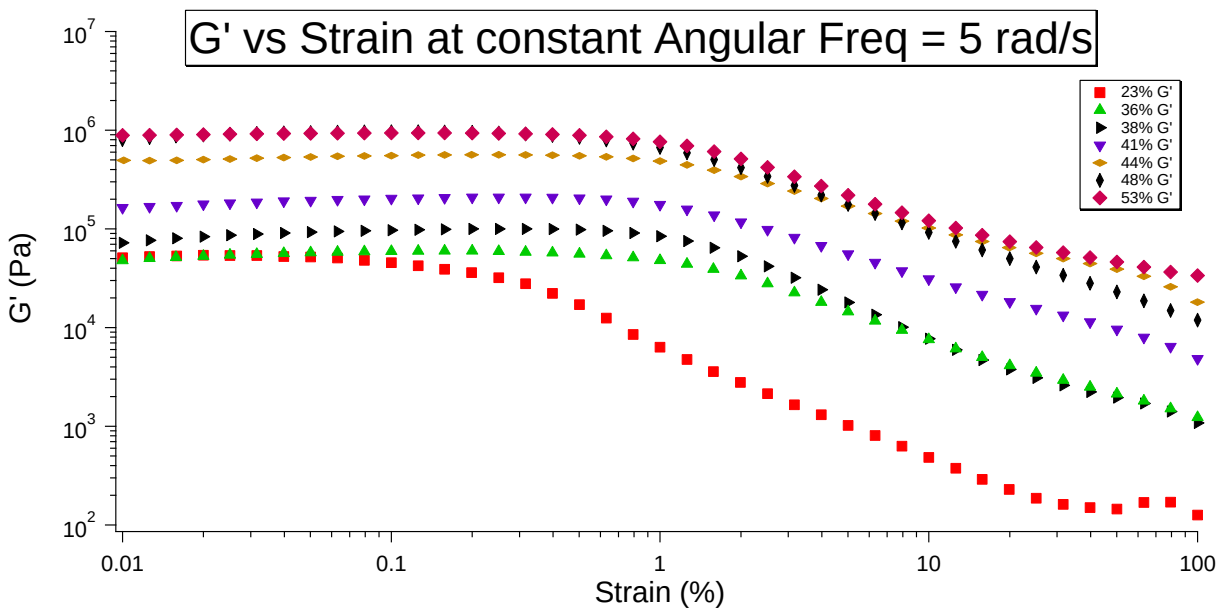

b)

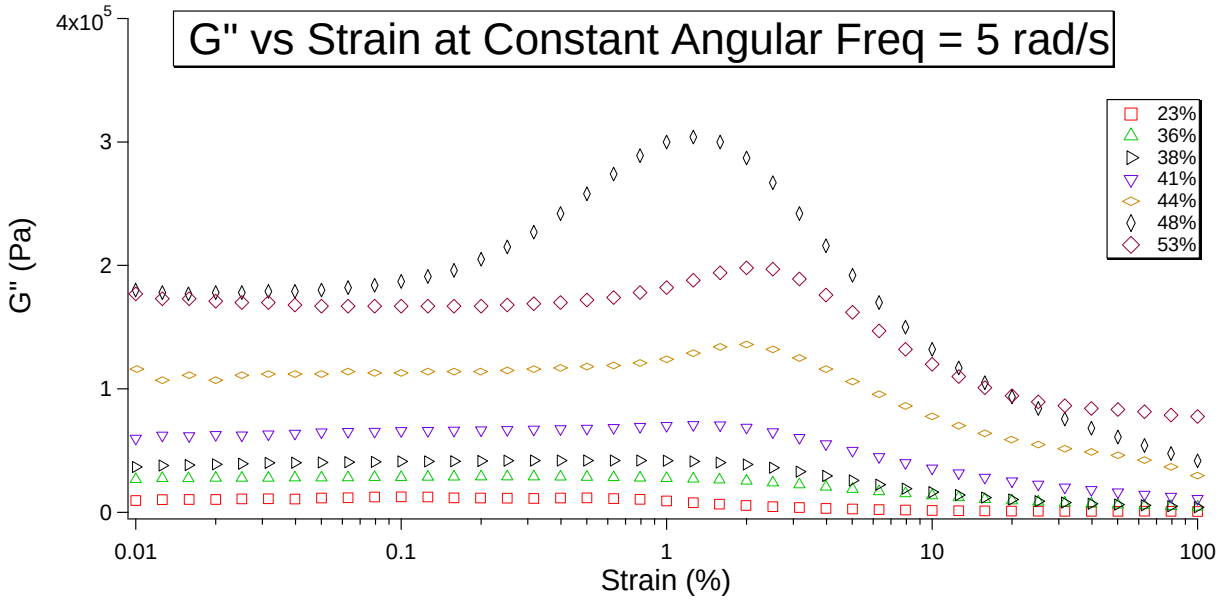

Figure 8

3.7 SEM and EDX

Analysis by Scanning Electron Microscopy (SEM, LEO 1550-FESEM) was performed to analyze the surface of post-mortem cells. SEM samples were prepared from post-mortem symmetric coin cells that underwent a polarization test. Coin cells were broken down in a glove box filled with inert argon gas and the lithium anode extracted. The anode was washed in PC to remove any tethered electrolyte that was not contained in the SEI layer. The sample was then evacuated in the glove box antechamber to evaporate the remaining propylene carbonate for 3 hours until dry. Following evaporation the samples were placed into a small plastic container sealed with parafilm to prevent oxidation during transport to the SEM facility.

Post-mortem analysis of the lithium electrode of symmetric coin cells after failure by polarization shows a cracked lithium surface with dendritic growth in certain areas, while other

areas appear to be smooth and unaffected by dendrites. It is theorized that uneven deposition of lithium metal produces seeds for lithium dendrite growth, and the tip of the dendrite during growth is led by a depletion zone that draws additional lithium ions. Eventually, this dendrite reaches the opposite electrode and leads to short circuit. Oppositely, a smooth lithium deposition should theoretically be able to fully stem dendritic growth. The images along with EDX data discussed later show evidence of the tethered electrolytes ability to smooth lithium deposition. A particularly strong indication of this is in Figure 9a where the dendrites appear to grow around the smoothed area, lifting the area off of the surface of the electrode. The image clearly shows that the smoothed area exhibits no dendritic growth and is able to prevent puncture from dendritic growth. This particular coin cell contained an electrolyte with a 48% particle loading run at a current density of 0.028 mA/cm^2.

Energy Dispersive X-Ray Spectroscopy (EDX) was done in tandem with SEM to analyze the chemical make-up of the dendritic and smooth regions of the post-mortem samples. Figure 9b shows EDX of the dendritic and smooth regions of the electrode along with the corresponding SEM image of the area of the electrode under investigation. EDX performed on the dendritic region showed only peaks of oxygen and carbon. Lithium is known to readily oxidize when exposed to air and the larger oxygen peak is a result of a combination of lithium oxidation and the oxygen found in the propylene carbonate additive. The carbon peak is purely from the residual propylene carbonate left on the lithium anode after the anode was dried. EDX performed on the smooth region, however, shows large peaks in carbon, oxygen, fluorine, silicon, and a small nitrogen peak just below .40 keV, obtained from an SEI layer containing the silica nanoparticle tethered to the piperidinium ionic liquid with the TFSI anion. This data along with the SEM images show that an SEI layer containing the tethered electrolyte is able to smooth

lithium deposition and prevent puncturing by dendritic growth. This could be due to the lowering of the overpotential for lithium plating and stripping that prevents dendritic growth as well as a mechanical suppression from the rigid particle network within the SEI layer that acts as a physical barrier. However, as it can be seen that lithium dendrites are still able to propagate, it is not yet enough to say that this smoothing of lithium deposition is enough to completely prevent dendritic growth.

a)

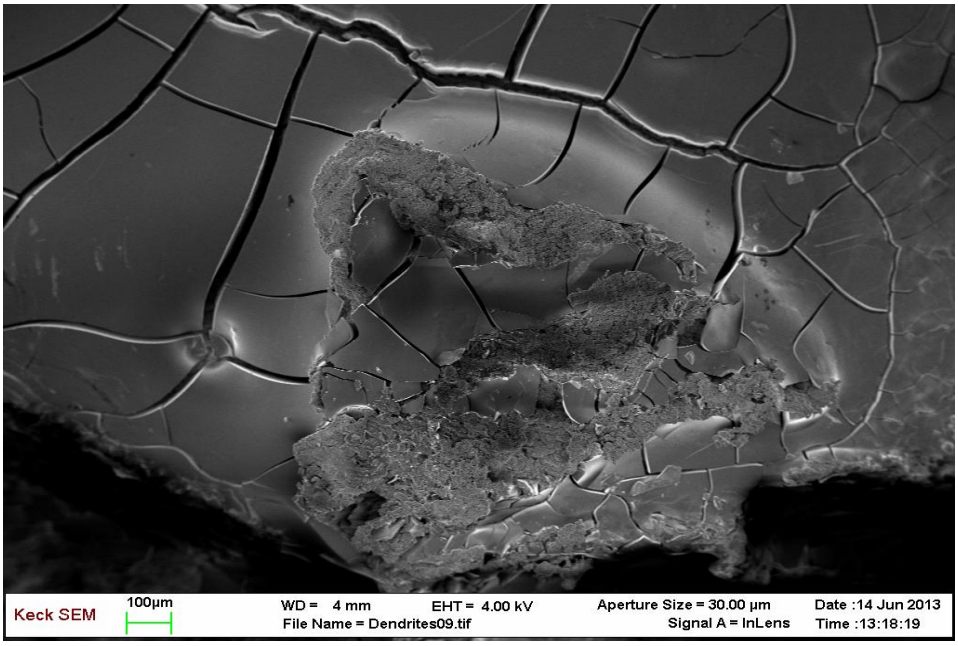

b)

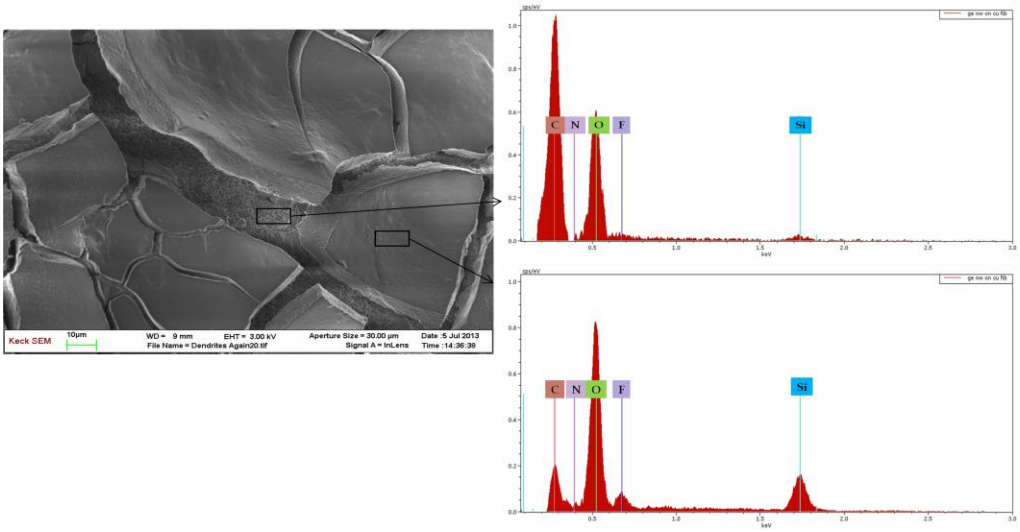

Figure 9

3.8 Symmetric Cell Experiments

Short circuit times were determined from polarization experiments run in lithium symmetric cells. The electrolytic cells were run at current densities ranging from 0.028 to 0.848 mA/cm^2, current densities that were below the limiting current. Three identical symmetric cells were run for each loading at each current density for accuracy. From the potential profiles, it can be seen that the potential initially increases and is then quickly followed by a drop in potential when run at a current densities that are closer to the limiting current. The drop is thought to be caused by a shorter effective inter electrode distance when the dendrite is growing,[10] which in turn indicates that the dendrite grows quickly after the polarization experiment begins. The quick onset of dendrite growth could be caused by surface roughening when preparing the lithium electrodes, which would leave seeds for dendrite growth. Following the initial drop in voltage, the voltage then begins to rise again, indicating an increase in resistance of the cell. This rise in resistance may be caused by a loss of electrolyte over time when polarized in a symmetric cell,

as no such electrolyte degradation is evident when run against a LTO electrode. This is further explained in the next section. The short circuit time was taken as the first significant drop in potential that stayed at a low potential for a prolonged period of time or was followed by a sporadic voltage profile. The sporadic voltage profile following the short denotes a series of dendrite shorts that continually melt and short circuit the cell. When the first dendrite short circuits the cell, the amount of current running through a single dendrite causes the dendrite to melt. This repeats until the major front of dendrites reach the opposite electrode and the cell becomes permanently short circuited. Using this knowledge combined with the fact that the inter electrode distance is shortened by a growing dendrite, the potential will plummet to a certain point at which it will short circuit, the potential will drop significantly, the dendrite will eventually melt, and the potential will return to a level that is in the neighborhood of what it was before the short. The sporadic voltage profile produced is thought to be caused by this phenomenon.

Figure 10d shows the short circuit times for the symmetric cells. There is some scattering in the data making it difficult to come up with viable conclusions. Theory states that higher current densities will decrease the time to the onset of dendrite growth and thus short circuit quicker. From the data it can be seen that the short circuit time for the electrolyte with 23% loading increases when going from 0.085 to 0.141 mA/cm^2 and the short circuit time for the electrolyte with 44% loading increases when going from 0.028 to 0.085 mA/cm^2, results that are unexpected. Despite this, it can be seen that there is a general trend that shows a decreasing short circuit time with increasing current density showing a slope of around -1. The -2 slope predicted by the Sand's time equation is not reached here, similar to results obtained by other members of the group, which may suggest that other mechanisms could contribute to the onset of dendritic

growth.[41] The short circuit time results for the highest current density was unable to be graphed for the 44% loading because it failed in the high current density regime. This is due to the lower conductivity at higher particle loading electrolytes that make the electrolyte less able to transport ions back to relieve the space charge region at higher current densities.

a)

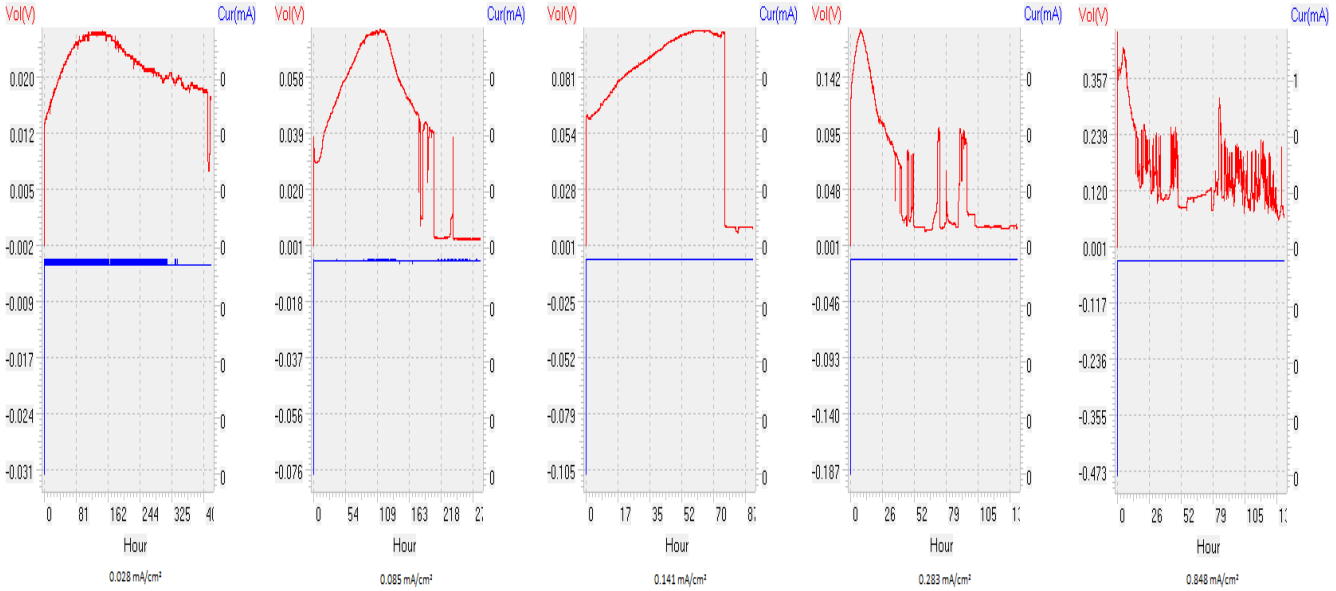

b)

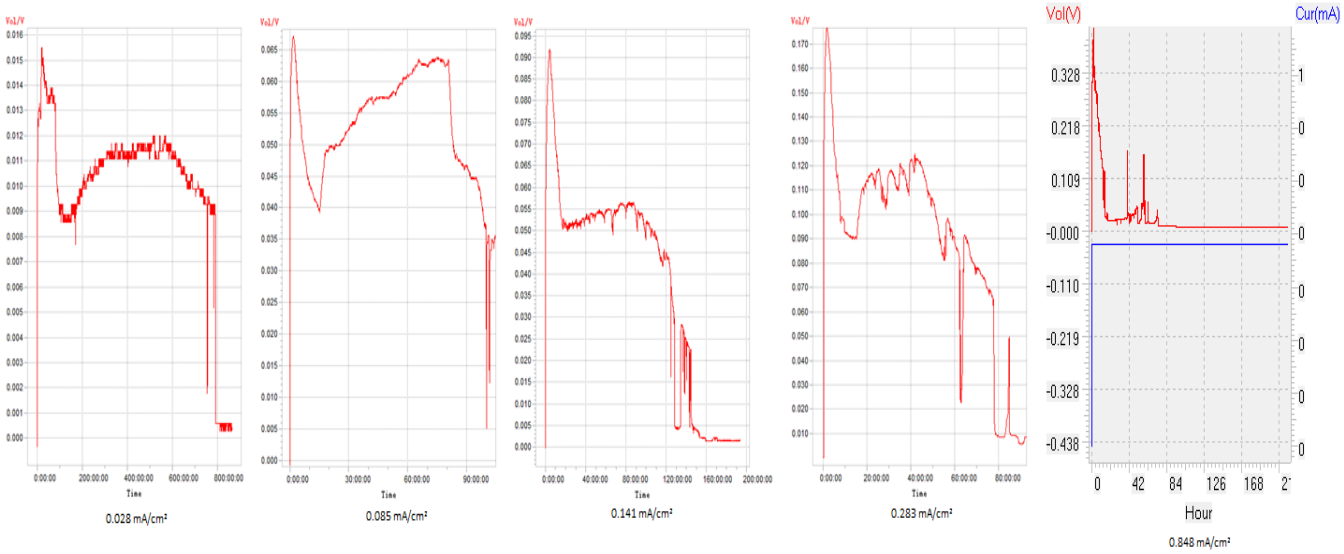

c)

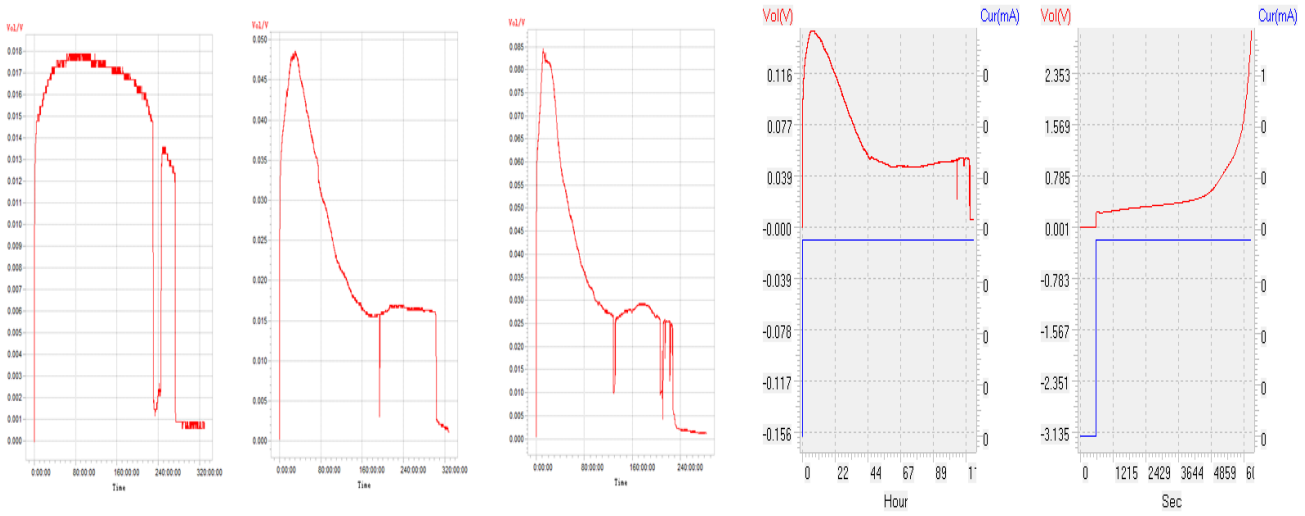

d)

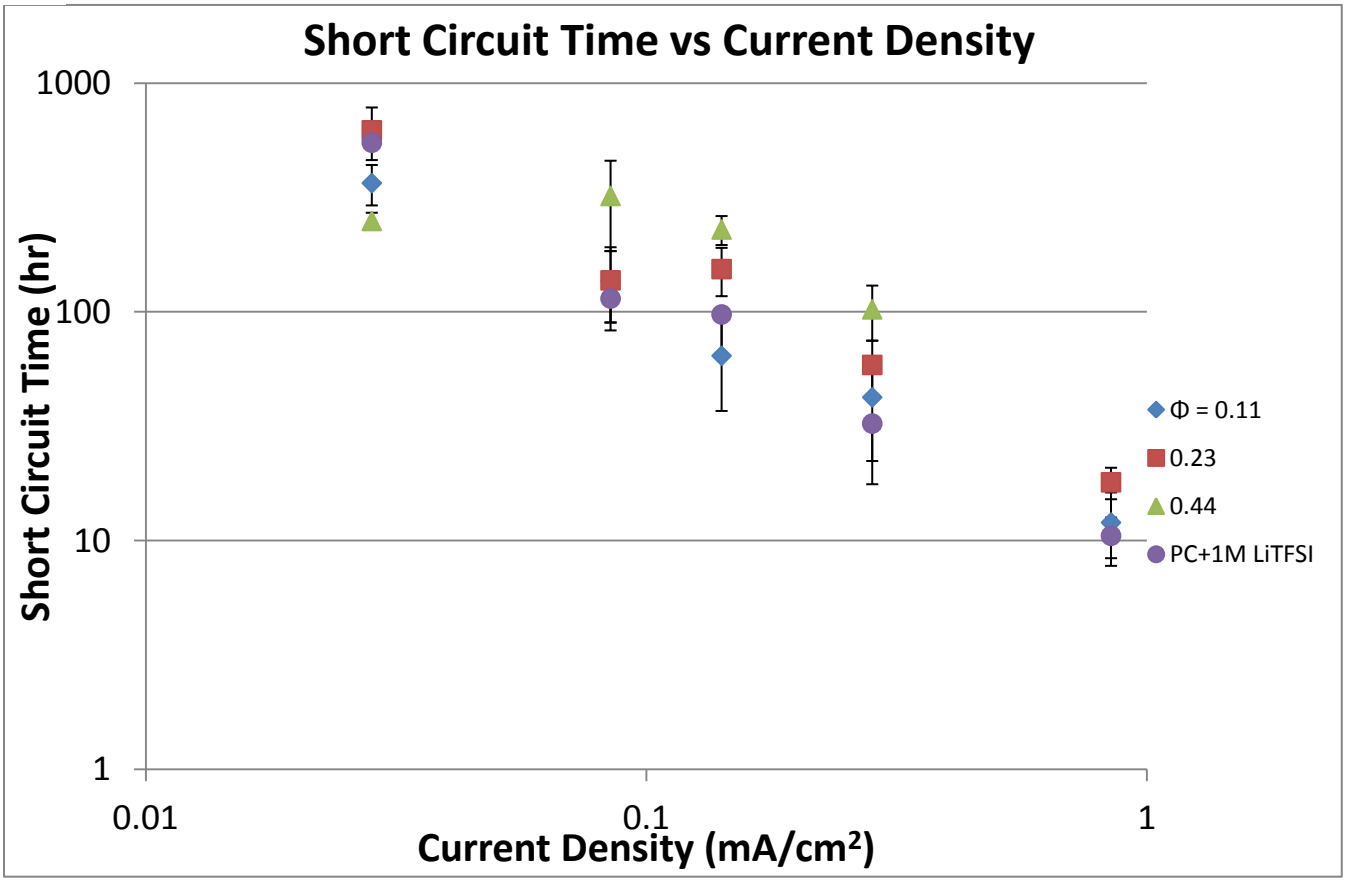

Figure 10: Polarization profiles of lithium symmetric cells with the a) 11% b) 23% c) 44% particle loadings and d) graph of short circuit times

Cycling experiments were performed on lithium symmetric cells run at 1 mA/cm^2 for 20 minutes each half cycle to mimic the cycling of a battery run at a 3C rate. The cycling profiles further suggest that the electrolyte may be lost over time as the current is passed through the symmetric cell. In each of the 11%, 23%, and 44% particle loadings of the tethered electrolyte, the cycling data show a rise in voltage over time, also suggesting a rise in resistance of the cell. Particularly indicative of this is the 44% tethered electrolyte profile that shows spikes in voltage and a very sporadic cycling profile. The jammed structure of this electrolyte solution disallows quick flow of the electrolyte, so when the electrolyte is lost, it creates pockets of electrolyte degradation products, which is hypothesized to be areas of massive resistance, leading to the spikes in potential profile. Further work must be performed to verify this phenomenon.

It is important to note that a cycling experiment tend to be a less aggressive test than the polarization experiment. Comparing the results in the rightmost image in Figure 10a to those in the leftmost image in Figure 11, which are cells that are run at a very similar current density, it can be seen that short circuit occurs in roughly 20 hours in the polarization experiment whereas the cycling experiment shows no signs of short circuit even after 1000 hours had passed. This is because at the beginning of every half cycle in the cycling experiment, the space charge region that was formed is relieved and must reform when the current direction is switched, whereas in the polarization experiment the space charge region is a constant stress on the system. However experiments, both have their merits in measuring the properties of the system. The polarization experiment measures the extreme case of infinite charge time, where the lithium ions only travel in one direction in the cell and tend to pile up once uneven lithium deposition begins. The cycling experiment is more representative of how a cell will perform in the real world, where cell are discharged and charged a few times a day. Both experiments are important to fully

understand the capabilities of the battery cell when using the tethered electrolyte as the electrolyte.

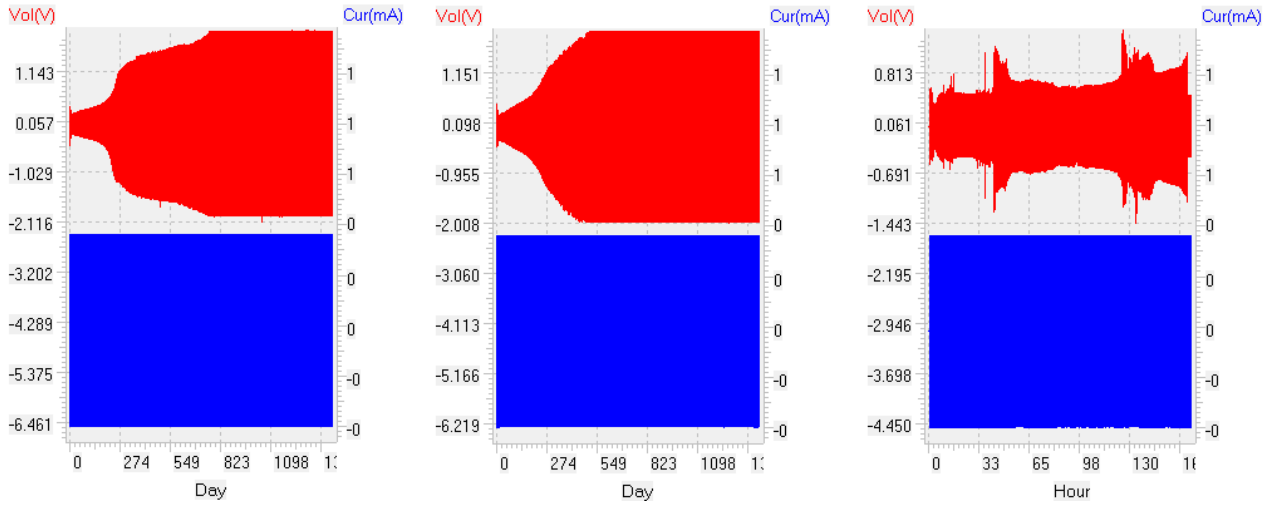

Figure 11: Left to Right: 11%, 23%, and 44% loadings

3.9 Full Cell Battery Experiments

Capacity tests were performed on full cell batteries with lithium metal as the anode and a carbon modified lithium titanate (LTO) cathode that contained 5% vapor grown carbon fiber and 5% carbon black. LTO is known to have a lower capacity, a theoretical 175 mAh/g, but is able to withstand high current densities for quick charging.[38] This cathode was said to exhibit 20% improvement in capacity over LTO electrodes that solely contained either of the two carbon materials[8]. Each cell was run at a 3C rate that was calculated using the 175 mAh/g theoretical capacity and each individual LTO electrode weight.

In Figure 12, the capacity vs cycle data can be seen. Figure 12a shows that the 11% tethered electrolyte exhibits stable capacity up to around 1200 cycles before its capacity begins to fade. The electrolyte retains a coulombic efficiency of 87% after 1000 cycles, representing excellent cycle life, and even after the capacity fade at 2000 cycles, the cell still retains 63% of its initial capacity. In Figure 12b, the 23% electrolyte exhibits a coulombic efficiency of 85% at 1000 cycles. After 2000 cycles, the capacity remains above 50% of its initial. Capacity fades in lithium ion batteries are associated with decomposition of the electrolyte, lithium dissolution, passive film formation, and many other phenomenon.[39] SEI formation is known to occur within the first few cycles, shown in the initial capacity loss in both electrolytes.

a)

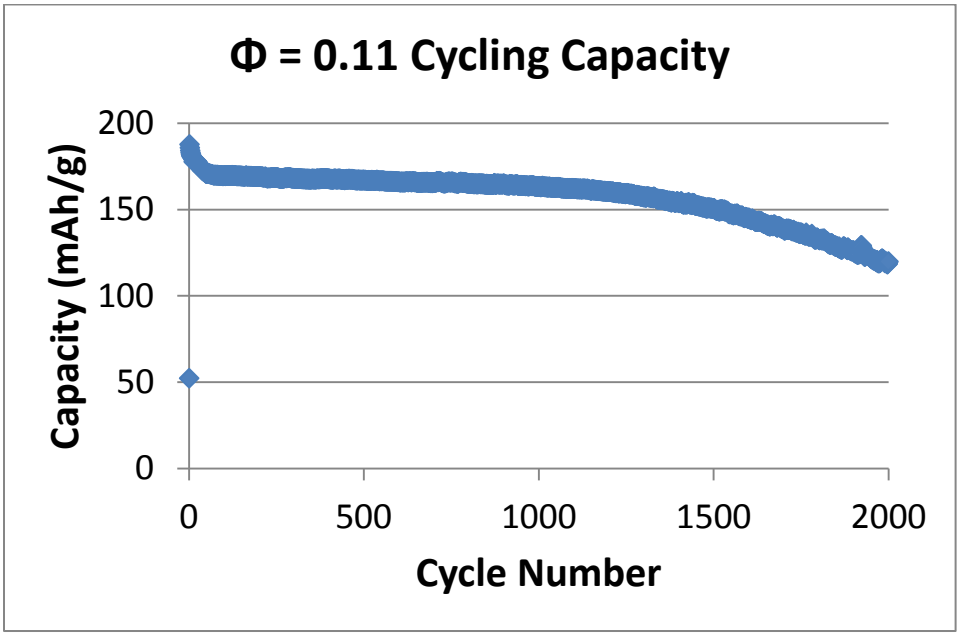

b)

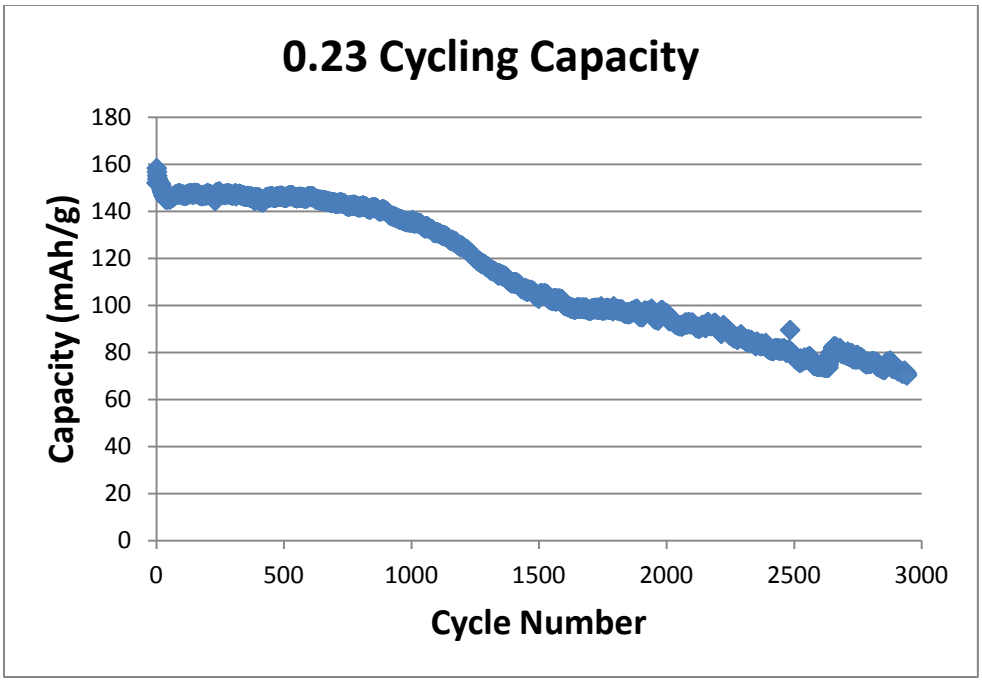

Figure 12

The charge-discharge profiles of both the 11% and the 23% tethered electrolyte are shown in Figure 13. Both particle loadings show stable voltage plateaus for over 1000 cycles when cycled at a 3C rate, suggesting that there is minimal degradation of the electrolyte or reactions occurring within the cell. However, the charge/discharge curves at the 2000th cycle have voltage plateaus that deviate from those of the previous cycles, indicating electrolyte decomposition and leading to subsequent large capacity loss. It seems that the LTO electrode is able to stabilize the electrolyte for a longer period of time than the symmetric cell, which is shown in Figure 11 and reveals electrolyte decomposition very quickly after cycling began. This stabilization might be due to contributions of a lithium titanate electrode that is known to be a zero insertion-strain material, allowing it to exhibit a negligible overvoltage and is thus able to stem electrolyte reaction and decomposition.[42]

It is noteworthy that even after 2000 cycles in both the 11% and 23% tethered electrolyte cells, the cycling profiles displayed no sign of short circuit. This further demonstrates the electrolyte's ability to stem lithium dendrite growth in a real battery environment. Hurdling this major obstacle that has plagued lithium metal batteries is a major step forward. This paired with the large capacity retention by the cycled cells demonstrates the piperidinium tethered electrolyte's potential for future use in secondary lithium batteries.

a)

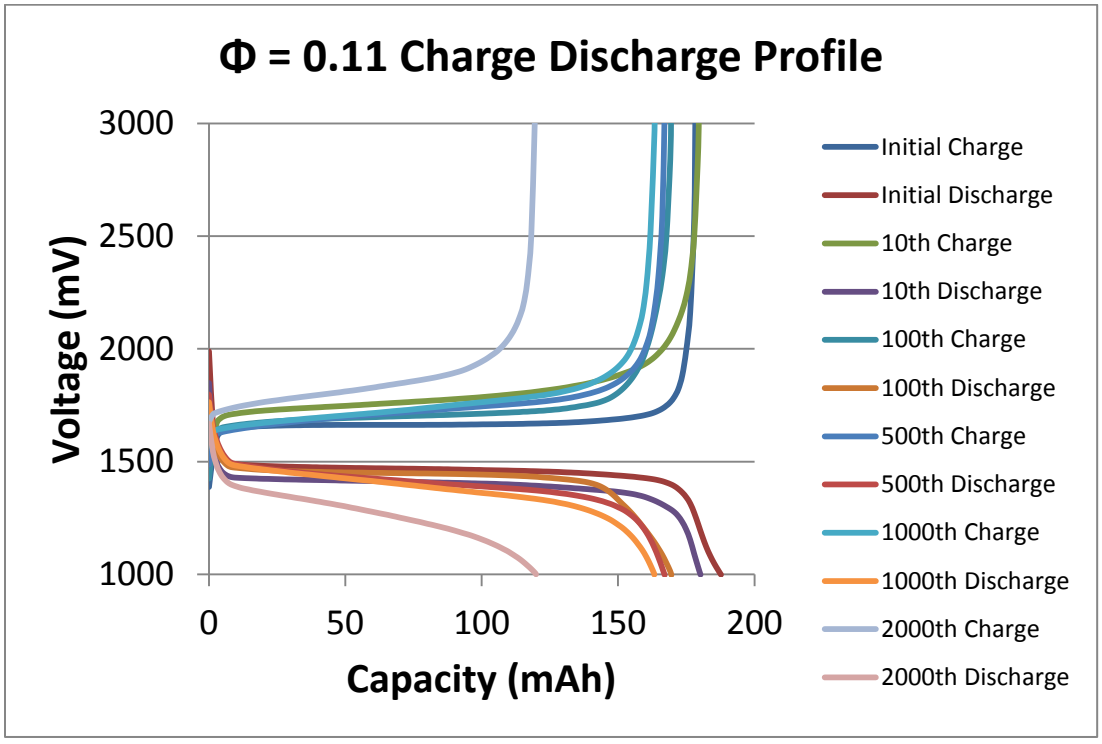

b)

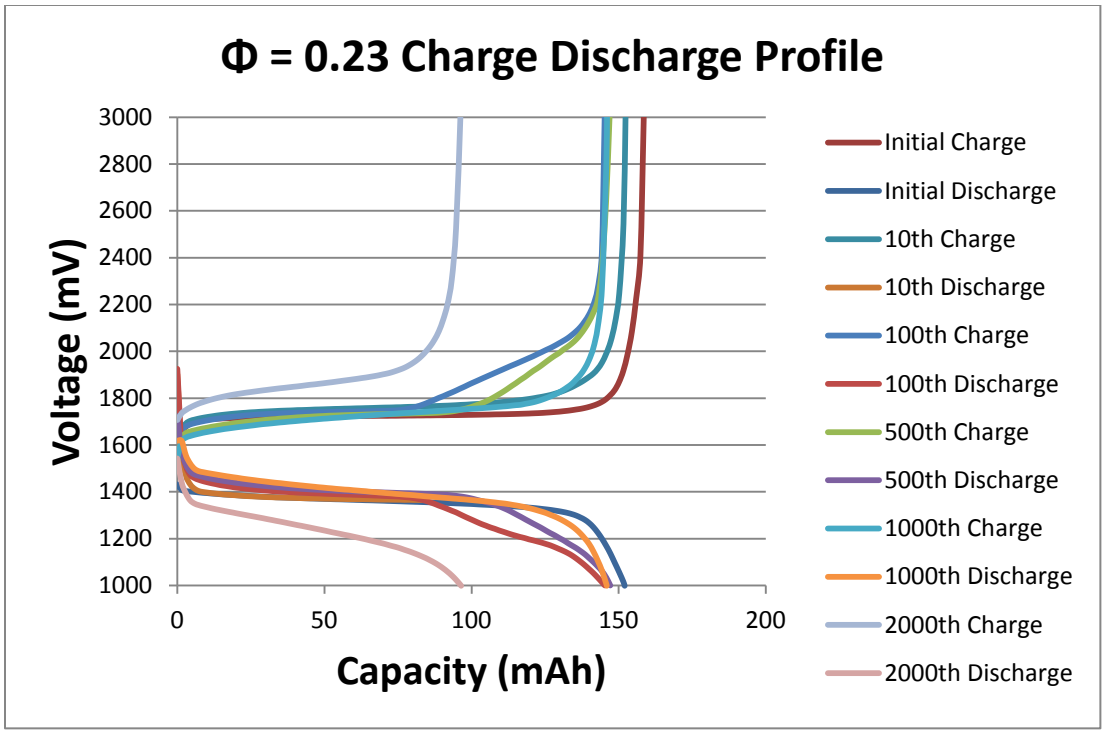
Φ = 0.23 Charge Discharge Profile
Voltage (mV)
3000
2800
2600
2400
2200
2000
1800
1600
1400
1200
1000
0
50
100
150
200
Capacity (mAh)
Initial Charge
Initial Discharge
10th Charge
10th Discharge
100th Charge
100th Discharge
500th Charge
500th Discharge
1000th Charge
1000th Discharge
2000th Charge
2000th Discharge

Figure 13

CHAPTER 4

CONCLUSION

This report details the properties and battery performance of a novel electrolyte consisting of piperidinium tethered silica nanoparticles, PC, and 1M LiTFSI. It was shown that the electrolyte displayed thermal stability up to 380 °C, high conductivities that were weakly affected by increases in viscosity and followed a VFT fit, lower interfacial resistances than its free ionic liquid counterparts, and could be tuned to exhibit MPa scale moduli due to the jamming phase transition. SEM data showed that the SEI layers formed by the electrolyte in cycled lithium symmetric cells contained constituents of the electrolyte and was able to stem dendritic growth. Polarization experiments revealed cells that lasted up to 800 hours before short circuit but polarization profiles showed a quick onset of dendritic growth. Symmetric cell cycling experiments run at a 1 mA/cm2 rate showed what is hypothesized to be a loss of electrolyte over time but exhibited no short circuit even after 1000 hours. Battery tests on LTO/glass fiber + tethered electrolyte/Li cells run at a 3C rate showed capacity retentions of up to 87% after 1000 cycles for both the 11% and 23% tethered electrolyte with the tethered electrolyte maintaining chemical robustness throughout cell operation that might be due to the LTO counterelectrode. The piperidinium based tethered electrolyte requires work to fully understand the mechanisms governing its limitations as an electrolyte but shows promise for use in future lithium metal batteries.

REFERENCES

1. Jin, Bo, Kim, Jong-Uk, Gu, Hal-Bon, Electrochemical Properties of Lithium-sulfur Batteries. J. Power Sources **117**, 148-152, (2003).
2. Girishkumar, G., McCloskey, B., Luntz, A.C., Swanson, S., Wilcke, W., Lithium-Air Battery: Promise and Challenges, J. Phys, Chem. Lett. **1**, 2194-2203, (2010).
3. Tarascon, J.-M., Armand, M., Issues and Challenges Facing Rechargeable Lithium Batteries, Nature **414**, 359-367, (2001).
4. Bruce, Peter G., Scrosati, Bruno, Tarascon, Jean-Marie, Nanomaterials for Rechargable Lithium Batteries, Angew. Chem. Int. Ed. **47**, 2930-2946 (2008).
5. Bruce, Peter G., Freunberger, Stefan A., Hardwick, Laurence J., Tarascon, Jean-Marie, Li-O_2 and Li-S batteries with high energy storage, Nature **11**, 19-29 (2011).
6. Liu, S., Imanishi, N., Zhang, T., Hirano, A., Takeda, Y., Yamamoto, O., Yang, J., Lithium Dendrite Formation in Li/Poly(ethylene oxide)-Lithium Bis(trifluoromethanesulfonyl)imide and N-methyl-N-propylpiperidinium Bis(trifluoromethanesulfonyl)imide/Li Cells, J. ECS **157**, A1092-A1098 (2010).
7. Porter, Ned A., Caldwell, Sarah E., Mill, Karen A. Mechanisms of Free Radical Oxidation of Unsaturated Lipids. Lipids **30**, 277-290(1995).
8. Kambe, Yu, Fernandez, Alberto J., Archer, Lynden A., Effects of Vapor Grown Carbon Fiber Substitution for Conductive Carbon in Anode Systems for LiB Applications. MRS Online Proceedings Library **1541**, (2013).
9. Aurbach, Doron, Zinigrad, Ella, Yaron, Cohen, Teller Hanan, A short review of failure mechanisms of lithium metal and lithiated graphite anodes in liquid electrolyte solutions, Solid State Ionics **148**, 405-416 (2002).

10. Chazalviel, J.-N., Electrochemical aspects of the generation of ramified metallic electrodeposits, Phys. Rev. A. **42**, 7355-7367 (1990).

11. Brissot, C., Rosso, M., Chazalviel, J.-N., Lascaud, S., Dendritic growth mechanisms in lithium/polymer cells. J. Power Sources **81-82**, 925-929 (1999) .

12. Lu, Yingying, Moganty, Surya S., Schaefer, Jennifer L., Archer, Lynden A., Ionic liquid-nanoparticle hybrid electrolytes. J. Mat. Chem. **22**, 4066-4072 (2012).

13. Kerr, J. B., Sloop, S. E., Liu, G., Han, Y. B., Hou, J., Wang, S., From molecular models to system analysis for lithium battery electrolytes, J. Power Sources **110**, 389-400 (2002).

14. Kim, Jae-Kwang, Matic, Alexander, Ahn, Jou-Hyeon, Jacobsson, Per, An imidazolium based ionic liquid electrolyte for lithium batteries, J. Power Sources **195**, 7639-7643 (2010).

15. Stone, G.M., Mullin, S. A., Teran, A. A., Hallinan Jr., D. T., Minor, A. M., Hexemer, A, Balsara, N. P., Resolution of the Modulus vesus Adhesion Dilemma in Solid Polymer Electrolytes for Rechargeable Lithium Metal Batteries, J ECS **159**, A222-A227 (2012).

16. Eshkenazi, V., Peled, E., Burstein, L., Golodnitsky, D., XPS analysis of the SEI formed on carbonaceous materials, Solid State Ionics **170**, 83-91 (2004).

17. Edström, Kristina, Herstedt, Marie, Abraham, Daniel P., A new look at the solid electrolyte interphase on graphite anodes in Li-ion batteries, J. Power Sources **153**, 380-384 (2006).

18. Lewandowski, Andrzej, Swiderska-Mocek, Agnieszka, Properties of the graphite-lithium anode in N-methyl-N-propylpiperidinium bis(trifluoromethanesulfonyl) imide as an electrolyte, J. Power Sources **171**, 938-943 (2007).

19. Lewandowski, Andrzej, Swiderska-Mocek, Agnieszka, Ionic liquids as electrolytes for Li-ion

batteries – An overview of electrochemical studies, J. Power Sources **194**, 601-609 (2009).

20. Galinski, Maciej, Lewandowski, Andrzej, Stepniak, Izabela, Ionic liquids as electrolytes, Electrochimica Acta **51**, 5567-5580 (2006).

21. Sakaebe, Hikari, Matsumoto, Hajime, N-Methyl-N-propylpiperidinium bis(trifluoromethanesulfonyl)imide (PP13-TFSI) – novel electrolyte base for Li battery, Electrochemistry Communications **5**, 594-598 (2003).

22. Liu, S., Imanishi, N., Zhang, T., Hirano, A., Takeda, Y., Yamamoto, O., Yang J., Effect of nano-silica filler in polymer electrolyte on Li dendrite formation in Li/poly(ethylene oxide)-Li$(CF_3SO_2)_2N$/Li, J. Power Sources **195**, 6847-6853 (2010).

23. Bourlinos, Athanasios B., Chowdhury, Subhendu Ray, Herrera, Rafael, Jiang, David D., Zhang, Qiang, Archer, Lynden A., Giannelis, Emmanuel P., Functionalized Nanostructures with Liquid-Like Behavior: Expanding the Gallery of Available Nanostructures, Adv. Funct. Mater. **15**, 1285-1290 (2005).

24. Ueno, K., Hata, K., Katakabe, T., Kondoh, M., Watanbe, M., Nanocomposite Ion Gels Based on Silica Nanoparticles and an Ionic Liquid: Ionic Transport, Viscoelastic Properties, and Microstructure, J. Phys. Chem. B **112**, 9013-9019 (2008).

25. Long, S., Howlett, P. C., MacFarlane, D. R., Forsyth, M., Fast ion conduction in an acid doped pentaglycerine plastic crystal. Solid State Ionics **117**, 647-652 (2006).

26. Monroe, Charles, Newman, John, Dendrite Growth in Lithium/Polymer Systems: A Propagation Model for Liquid Electrolytes under Galvanostatic Conditions, J ECS **150**, A1377-A1384 (2003).

27. Monroe, Charles, Newman, John, The Impact of Elastic Deformation on Deposition Kinetics

of Lithium/Polymer Interfaces, J ECS **152**, A396-A404 (2005).

28. Rosso, M., Gobron, T., Brissot, C., Chazalviel, J.-N., Lascaud, S., Onset of Dendrite growth in lithium/polymer cells, J. Power Sources **97-98**, 804-806 (2001).

29. Liu, S., Wang, H., Imanishi, N., Zhang, T., Hirano, A., Takeda, Y., Yamamoto, O., Yang, J., Effect of co-doping nano-silica filler and N-methyl-N-propylpiperidinium bis(trifluoromethanesulfonyl)imide into polymer electrolyte on Li dendrite formation in Li/poly(ethylene oxide)-Li(CF_3SO_2)$_2$N/Li, J. Power Sources **196**, 7681-7686 (2011).

30. Armand, Michel, Endres, Frank, Macfarlane, Douglas R., Ohno, Hiroyuki, Scrosati, Bruce. Ionic-liquid materials for the electrochemical challenges of the future, Nature **8**, 621-629 (2009).

31. Zhou, Feng, Liang, Yongmin, Liu, Weimin, Ionic Liquid lubricants: designed chemistry for engineering applications, Chem. Soc. Rev. **38**, 2590-2599 (2009).

32. Lu, Jianmei, Yan, Feng, Texter, John, Advanced applications of ionic liquids in polymer science, Prog. Polym. Sci **34**, 431-448 (2009).

33. Morris, Russell E., Ionothermal synthesis – ionic liquids as functional solvents in the preparation of crystalline materials.

34. Duluard, Sandrine, Grondin, Joseph, Bruneel, Jean-Luc, Pianet, Isabelle, Grélard, Axelle, Campet, Guy, Delville, Marie-Hélène, Lassègues, Lithium solvation and diffusion in the 1-butyl-3-methylimidazolium bis(trifluoromethanesulfonyl)imide ionic liquid, J. Raman Spectrosc. **39**, 627-632 (2008).

35. Saito, Yuria, Umecky, Tatsuya, Niwa, Junichi, Sakai, Tetsuo, Maeda, Seiji, Existing

Condition and Migration Property of Ions in Lithium Electrolytes with Ionic Liquid Solvent, J. Phys. Chem. B **111**, 11794-11802 (2007).

36. Frömling, T., Kunze, M., Schönhoff, M., Sundermeyer, J., Roling, B., Enhanced Lithium Transference Numbers in Ionic Liquid Electrolytes, J. Phys. Chem. B. **112**, 12985-12990 (2008).

37. Bruce, Peter G., Evans, James, Vincent, Colin A., Conductivity and Transference Number Measurements on Polymer Electrolytes, Solid State Ionics **28-30**, 918-922 (1988).

38. Nakahara, Kiyoshi, Nakajima, Ryosuke, Matsushima, Tomoko, Majima, Hiroshi, Preparation of particulate $Li_4Ti_5O_{12}$ having excellent characteristics as an electrode active material for power storage cells, J. Power Sources **117**, 131-136 (2003).

39. Arora, Pankaj, White, Ralph E., Doyle, Marc, Capacity Fade Mechanisms and Side Reactions in Lithium-Ion Batteries, J. Electrochem. Soc. **145**, 3657-3667 (1998).

40. Moganty, Surya S., Jayaprakash, N., Nugent, Jennifer L., Shen, J., Archer, Lynden A., Ionic Liquid-Tethered Nanoparticles: Hybrid Electrolytes, Angew. Chem. **122**, 9344-9347 (2010).

41. Lu, Yingying, Das, Shyamal K., Moganty, Surya S., Archer, Lynden A., Ionic Liquid-Nanoparticle Hybrid Electrolytes and their Application in Secondary Lithium-Metal Batteries, Adv. Mater., 1-6 (2012).

42. Sawai, Keijiro, Yamato, Ryoji, Ohzuku, Tsutomu, Impedance Measurements on lithium-ion battery consisting of $Li[Li_{1/3}Ti_{5/3}]O_4$ and $LiCo_{1/2}Ni_{1/2}O_2$, Electrochimica Acta **51**, 1651-1655 (2006).